Impacts of black carbon mixing state on black carbon nucleation scavenging: Insights from a particle-resolved model

J. Ching,[1] N. Riemer,[1] and M. West[2]

Received 8 June 2012; revised 4 October 2012; accepted 22 October 2012; published 14 December 2012.

[1] This paper presents an advancement of the recently developed particle-resolved aerosol model PartMC-MOSAIC (Particle Monte Carlo-Model for Simulating Aerosol Interactions and Chemistry) to investigate the impacts of mixing state on cloud droplet formation and to provide a tool for the quantification of errors in cloud properties introduced by simplifying mixing state assumptions. We coupled PartMC-MOSAIC with a cloud parcel model. We initialized the cloud parcel simulation with hourly PartMC-MOSAIC model output from a 48-hour urban plume simulation. The cloud parcel model then explicitly simulated activation and condensational growth of the particles as the parcel underwent cooling at a specified rate and the particles of the aerosol population competed for water vapor. We used this capability to quantify the relative importance of size information versus composition information for the prediction of the cloud droplet number fraction, mass fraction of black carbon that is nucleation-scavenged, cloud droplet effective radius, and relative dispersion of the droplet size distribution by introducing averaging of particle-resolved information within prescribed bins. For the cloud droplet number fraction, both composition averaging and size-bin averaging individually led to an error of less than 25% for all cloud parcel simulations, while averaging in both size bins and composition resulted in errors of up to 34% for the base case cooling rate of 0.5 K/min. In contrast, for the nucleation-scavenged black carbon mass fraction, the results for size-bin averaging tracked the reference case well, while composition averaging, with or without size-bin averaging, led to overestimation of this quantity by up to 600%.

Citation: Ching, J., N. Riemer, and M. West (2012), Impacts of black carbon mixing state on black carbon nucleation scavenging: Insights from a particle-resolved model, *J. Geophys. Res.*, *117*, D23209, doi:10.1029/2012JD018269.

1. Introduction

[2] Black-carbon-containing aerosol particles are important for regional and global climate [*Forster et al.*, 2007]. They both absorb and scatter light, thereby reducing the solar radiation at the Earth's surface, and heating the atmosphere where they reside. Like other aerosol particles, black-carbon-containing particles can also serve as cloud condensation nuclei [*Hitzenberger et al.*, 1999] or ice nuclei [*DeMott et al.*, 1999; *Möhler et al.*, 2005], and hence impact the cloud microphysical properties as well as the cloud lifetimes. Their ability to absorb radiation has several additional consequences regarding their interaction with clouds. When embedded in or near a cloud layer, black-carbon-containing aerosols may heat the layer and cause cloud evaporation [*Hansen et al.*, 1997]. Furthermore, they can impact the stability of the atmosphere and hence vertical motions, which, in turn, impact cloud development. Depending on the relative altitude of the black-carbon-containing particles and the cloud, their presence can lead to enhanced convection, causing a cloud increase, or suppression of cloud formation, causing a cloud reduction [*Koch and Genio*, 2010]. These complex interplays contribute to the large uncertainties associated with the predictions of the net impact of black carbon mitigation [*Chen et al.*, 2010; *Spracklen et al.*, 2011; *Bahadur et al.*, 2012].

[3] Adding complexity is the fact that the optical properties and the cloud condensation nuclei and ice nuclei properties depend on the distribution of the per-particle composition of the black-carbon-containing aerosol, the so-called black carbon mixing state. Optical properties also depend crucially on the particle morphology and shape [*Adachi et al.*, 2010]. These properties in turn change continuously during the particles' lifetime. Upon emission, the black carbon content and the presence of other constituents depend strongly on the type of source [*Schwarz et al.*, 2008]. In this paper we focus on vehicle emissions from gasoline and diesel cars. Measurements show that the emitted particles from these sources are a complex mixture of many chemical species with the main constituents being black carbon and organic carbon [*Medalia and Rivin*, 1982; *Toner*

[1]Department of Atmospheric Sciences, University of Illinois at Urbana-Champaign, Urbana, Illinois, USA.
[2]Department of Mechanical Science and Engineering, University of Illinois at Urbana-Champaign, Urbana, Illinois, USA.

Corresponding author: N. Riemer, Department of Atmospheric Sciences, University of Illinois at Urbana-Champaign, 105 S. Gregory St., Urbana, IL 61801, USA. (nriemer@illinois.edu)

0148-0227/12/2012JD018269

et al., 2006], and trace concentrations of ionic and metallic species [*Kleeman et al.*, 2000]. During transport in the atmosphere, the particles' compositions change further as a result of physical processes such as coagulation with other particles and condensation of secondary aerosol species, or as a result of chemical processes.

[4] Along with these changes in composition, collectively termed "aging", go changes in both hygroscopicity and optical properties. *Weingartner et al.* [1997] concluded from their laboratory studies that freshly emitted combustion particles were unlikely to act as cloud condensation nuclei, whereas aging of the particles would improve their nucleation ability. Several recent field studies have confirmed this finding and show that the timescale of conversion from freshly emitted, hydrophobic black-carbon-containing particle to hydrophilic particle can be as low as a few hours during daytime [*Wang et al.*, 2010; *Moffet and Prather*, 2009], consistent with modeling studies by *Riemer et al.* [2004] and *Riemer et al.* [2010].

[5] Hence, to assess the budget of black carbon and its climate impact, it is important that regional and global models capture the evolution of the black carbon mixing state adequately [*Croft et al.*, 2005]. This is challenging, since, from a computational standpoint, resolving the mixing state ideally requires representing a multidimensional size distribution. Recently *Riemer et al.* [2009] developed PartMC-MOSAIC (Particle Monte Carlo-Model for Simulating Aerosol Interactions and Chemistry) for atmospheric aerosol applications. This stochastic particle-resolved model explicitly resolves the composition of individual aerosol particles in a given population of different particle types. Particle-based methods are efficient in resolving a multidimensional particle distribution as they scale with the number of particles, not with the number of dimensions.

[6] PartMC simulates particle emissions, dilution with the background, and Brownian coagulation stochastically by generating a realization of a Poisson process. Gas- and aerosol-phase chemistry (including the gas-particle partitioning, calculation of activity coefficients, and intra-particle solid-liquid partitioning) are implemented deterministically by coupling with the MOSAIC chemistry code [*Zaveri et al.*, 2008]. Since individual particles are explicitly tracked, there is no need to invoke ad hoc aging criteria that move aerosol mass between bins or modes as is the case with traditional modal or sectional approaches [*Riemer et al.*, 2003; *Stier et al.*, 2005; *Bauer et al.*, 2008; *Jacobson*, 2001]. It also completely eliminates any errors associated with numerical diffusion, which is useful when investigating conditions where rapid condensation occurs.

[7] In this paper we extended the capabilities of PartMC-MOSAIC by adding a cloud parcel module, which allows competition between the aerosol particles for water vapor as the air parcel experiences cooling. With this, we investigated the impacts of mixing state on cloud droplet formation. Throughout the past decades, cloud parcel models have been widely used for process studies to investigate the fundamentals relating to the drop size evolution and the factors that shape the cloud drop size spectrum [*Howell*, 1949; *Mordy*, 1959; *Lee et al.*, 1980; *Nenes et al.*, 2001; *Conant et al.*, 2004]. They have also been applied to investigate the interplay of cloud microphysics and chemistry [*Nenes et al.*, 2002; *Kreidenweis et al.*, 2003; *Ervens et al.*, 2005] and to derive parameterizations for larger scale models [*Ghan et al.*, 1993, 1995; *Abdul-Razzak et al.*, 1998; *Abdul-Razzak and Ghan*, 2000; *Nenes and Seinfeld*, 2003; *Fountoukis and Nenes*, 2005; *Segal and Khain*, 2006; *Ming et al.*, 2006].

[8] The contribution of this work is that the cloud parcel model is initialized with an aerosol population where the mixing state is fully resolved on a per-particle basis. It therefore simulates the competition of the particles for water vapor without any simplifying assumption about composition, and the numerical solution is not subject to numerical diffusion. As shown in this paper, this model framework can then be used to systematically quantify the importance of black carbon mixing state for cloud droplet formation, contrasting the importance of size information versus the importance of composition information.

[9] Section 2 introduces the model system and the associated numerical methods. The setup of the simulations used in this paper is described in Section 3. Section 4 presents the idealized plume scenario that served as a initialization for the cloud parcel simulations, which are described in Section 5. The simulation results are then used in Section 6 to quantify the importance of mixing state on cloud formation. Finally, we summarize our findings in Section 7.

2. Model Description

2.1. The Particle-Resolved Model PartMC-MOSAIC

[10] The governing model equations and the numerical algorithms of the particle-resolved model PartMC-MOSAIC are described in detail in *Riemer et al.* [2009]. Here we give a brief summary. In this paper we used PartMC version 2.1.0 and MOSAIC version 2011-01-10.

[11] We consider a Lagrangian parcel with volume V_{comp}, also called the computational volume. We represent the aerosol population by storing N_{p} particles that reside in this volume, written $\Pi = \left(\vec{v}_1, \vec{v}_2, \ldots, \vec{v}_{N_{\text{p}}}\right)$, where the particle order is not significant. Each particle is an A-dimensional vector $\vec{v}_i \in \mathbb{R}^A$ with components $\left(v_i^1, v_i^2, \ldots, v_i^A\right)$, so v_i^a is the volume of species a in particle i, for $a = 1, \ldots, A$ and $i = 1, \ldots, N_{\text{p}}$.

[12] The simulation proceeds by two mechanisms. First, the composition of each particle can change, changing the components of the vector $\vec{v}_i$ for particle i as species condense from the gas phase and evaporate to it. In this paper, gas-phase chemistry and gas-particle partitioning, calculation of activity coefficients, and intra-particle solid-liquid partitioning are treated deterministically by the MOSAIC model [*Zaveri et al.*, 2008]. The current version of MOSAIC treats all the locally and globally important gas phase and aerosol species. The gas phase photochemical mechanism used is the carbon bond mechanism CBM-Z [*Zaveri and Peters*, 1999], which includes 77 model species and 142 reactions. The aerosol species include SO_4, NO_3, Cl, CO_3, MSA (methanesulfonic acid), NH_4, Na, Ca, other inorganic mass (which includes species such as SiO_2, metal oxides, and other unmeasured or unknown inorganic species present in aerosols), black carbon (BC), primary organic aerosol (POA), and secondary organic aerosol (SOA). Three computationally efficient modules are used in conjunction with

CBM-Z, (1) the Multicomponent Taylor Expansion Method (MTEM) for estimating activity coefficients of electrolytes and ions in aqueous solutions [*Zaveri et al.*, 2005b]; (2) the Multicomponent Equilibrium Solver for Aerosols (MESA) for intraparticle solid-liquid partitioning [*Zaveri et al.*, 2005a]; and (3) the Adaptive Step Time-split Euler Method (ASTEM) for dynamic gas-particle partitioning over size- and composition-resolved aerosol [*Zaveri et al.*, 2008]. SOA is treated based on the Secondary Organic Aerosol Model (SORGAM) scheme [*Schell et al.*, 2001] and represented by four model species originating from the oxidation of anthropogenic VOC precursors (ARO1, ARO2, ALK1, OLE1), and four model species from the oxidation of biogenic VOC precursors (LIM1, LIM2, API1, API2).

[13] Second, the particle population Π can have particles added and removed, either by emissions, dilution or coagulation events between particles. While condensation/evaporation is handled deterministically, the efficient stochastic PartMC model [*Riemer et al.*, 2009] is used for emission, dilution, entrainment, and Brownian coagulation. In this paper PartMC explicitly represented every aerosol particle in the volume V_{comp}, corresponding to an unweighted simulation in the sense of *DeVille et al.* [2011].

2.2. Cloud Parcel Model

[14] In this section we describe the coupling of PartMC-MOSAIC with a cloud parcel model. To focus our simulations on the impacts of mixing state, we do not include any entrainment into the cloud parcel. Additionally, surface tension effects on droplet growth, sedimentation, and coagulation in the cloud parcel are not included.

[15] The system of ordinary differential equations that is solved for the cloud parcel is derived using classical Köhler theory [*Köhler*, 1936; *Seinfeld and Pandis*, 1997] adapted to the κ hygroscopicity parameterization [*Petters and Kreidenweis*, 2007]. The state of the system is described by the prognostic variables $\left(S_{\text{v}}, D_1, \ldots, D_{N_{\text{p}}}\right)$, where S_{v} is the environmental saturation ratio and D_i is the wet diameter of particle i, giving $N_{\text{p}} + 1$ variables in total. There are thus $N_{\text{p}} + 1$ corresponding differential equations, consisting of the condensational growth equation for each individual particle and the equation for the rate of change of environmental saturation ratio S_{v}.

[16] During the cloud parcel simulation, the constituent volumes v_i^a of each particle i are held fixed for each species a except water. We number the species so that water is the Ath species, and we write $v_i^{\text{w}} = v_i^A$ for the water volume in particle i. This varies with the wet diameter D_i according to

$$v_i^{\text{w}} = v_i - v_i^{\text{dry}}, \tag{1}$$

where $v_i = \frac{\pi}{6}(D_i)^3$ is the total volume and v_i^{dry} is the dry volume, obtained by summing the constituent species volumes over all non-water species, so that

$$v_i^{\text{dry}} = \sum_{i=1}^{A-1} v_i^a. \tag{2}$$

We will use these volumes below in the mixing rule assumptions for hygroscopicity parameters, as in *Petters and Kreidenweis* [2007].

[17] The condensational growth rate $\dot{D}_i$ of aerosol particle i is given by the solution to the pair of implicit equations:

$$\dot{D}_i = \frac{4D'_{\text{v},i} M_{\text{w}} P^0}{\rho_{\text{w}} R T D_i}\left(S_{\text{v}} - a_{\text{w},i}\frac{1}{1+\delta_i} \times \exp\left(\frac{4M_{\text{w}}\sigma_{\text{w}}}{\rho_{\text{w}} R T D_i}\frac{1}{1+\delta_i} + \frac{\Delta H_{\text{v}} M_{\text{w}}}{RT}\frac{\delta_i}{1+\delta_i}\right)\right) \tag{3}$$

$$\delta_i = \frac{\Delta H_{\text{v}} \rho_{\text{w}}}{4k'_{\text{a},i} T} D_i \dot{D}_i. \tag{4}$$

See *Seinfeld and Pandis* [1997] for a comprehensive derivation of these and other equations. Here, $D'_{\text{v},i}$ is the corrected diffusivity coefficient for particle i, $a_{\text{w},i}$ is the water activity of particle i, σ_{w} is the water surface tension, ΔH_{v} is the specific latent heat of vaporization of water, $k'_{\text{a},i}$ is the corrected thermal conductivity of air for particle i, T is the environmental temperature, ρ_{w} is the density of water, M_{w} is the molecular weight of water, R is the universal gas constant, and P^0 is the saturation vapor pressure. The formulations for $D'_{\text{v},i}$, $k'_{\text{a},i}$, and P^0 used here are given in section A1.

[18] We express the water activity $a_{\text{w},i}$ in equation (3) in terms of a dimensionless hygroscopicity parameter as was suggested by *Ghan et al.* [2001] and *Petters and Kreidenweis* [2007]. The latter authors termed this parameter κ, and we adopt this notation. The water activity is then given by

$$a_{\text{w},i} = \frac{v_i^{\text{w}}}{v_i^{\text{w}} + \kappa_i v_i^{\text{dry}}}. \tag{5}$$

For an aerosol particle i containing several non-water species, the κ_i value for the particle is the volume-weighted mean of the individual κ^a of each constituent species a [*Petters and Kreidenweis*, 2007], so

$$\kappa_i = \sum_{a=1}^{A-1} \kappa^a \frac{v_i^a}{v_i^{\text{dry}}}, \tag{6}$$

where the sum is over all non-water species (recalling that water is the Ath species). Following *Petters and Kreidenweis* [2007] and *Riemer et al.* [2010], we assumed $\kappa = 0.65$ for all salts formed from the NH_4^+-SO_4^{2-}-NO_3^- system. For all MOSAIC model species that represent secondary organic aerosol (SOA) we assumed $\kappa = 0.1$, based on measurements by *Prenni et al.* [2007]. Following *Petters et al.* [2006] we assumed $\kappa = 0.001$ for primary organic aerosol (POA) and $\kappa = 0$ for black carbon (BC). We do not consider sparingly soluble species [*Petters and Kreidenweis*, 2008] in this work (see section A2 for a discussion of why constant κ values were assumed).

[19] The rate of change of the environmental saturation ratio, $\dot{S}_{\text{v}}$, is the sum of the rate due to each particle and the rate due to temperature changes in the environment, giving

$$\dot{S}_{\text{v}} = -\sum_{i=1}^{N_{\text{p}}} \frac{\pi \rho_{\text{w}} R T}{2 M_{\text{w}} P^0 V_{\text{comp}}} D_i^2 \dot{D}_i - \frac{1}{P^0}\frac{\partial P^0}{\partial T} S_{\text{v}} \dot{T}, \tag{7}$$

where $\dot{T}$ is the prescribed rate-of-change of the temperature and we assume that the pressure is held constant. The

Table 1. Area Source Strength, E_a, of the Three Types of Emission and the Initial/Background Aerosol Population[a]

Initial/Background	N_a/cm^{-3}	$D_g/\mu m$	σ_g	Composition by Mass
Aitken mode	1800	0.02	1.45	49.64% $(NH_4)_2SO_4$ + 49.64% SOA + 0.72% BC
Accumulation mode	1500	0.116	1.65	49.64% $(NH_4)_2SO_4$ + 49.64% SOA + 0.72% BC
Emission	$E_a/m^{-2}\ s^{-1}$	$D_g/\mu m$	σ_g	Composition by Mass
Meat cooking	9×10^6	0.086	1.91	100% POA
Diesel Vehicles	1.6×10^8	0.05	1.74	30% POA + 70% BC
Gasoline Vehicles	5×10^7	0.05	1.74	80% POA + 20% BC

[a]The initial/background aerosol population size distribution is assumed to be lognormal and defined by the number concentration, N_a, the geometric mean diameter, D_g, and the geometric standard deviation, σ_g.

modeling approach used here follows *Majeed and Wexler* [2001] in prescribing the cooling rate. An alternative modeling framework would prescribe the updraft velocity and compute the temperature change. However, computing temperature changes would require the modeling of radiative heating effects [*Conant et al.*, 2002], which would significantly complicate the interpretation of our results. The pressure is kept constant for simplicity, following *Majeed and Wexler* [2001], as detailed reproduction of the updraft process is not relevant for this study.

[20] Here the computational volume, V_{comp}, starts at the initial value V_{comp}^0 and varies with environmental temperature as described by the law for ideal gases.

[21] The evolution of the water condensation dynamics is defined by equations (3), (4), and (7). In PartMC-MOSAIC these equations are solved numerically as described in section A3.

2.3. Critical Diameter and Critical Saturation

[22] In the following, we will frequently refer to the critical diameter and the critical supersaturation for the aerosol particles. To define these, we first find the equilibrium saturation ratio, $S_{e,i}$, for particle i by setting $\dot{D}_i = 0$ in (3) and (4). This gives

$$S_{e,i} = a_{w,i} \exp\left(\frac{4 M_w \sigma_w}{R T \rho_w D_i}\right). \quad (8)$$

The critical diameter, $D_{c,i}$, for particle i is the diameter that maximizes the equilibrium saturation ratio, and will be the unique solution of

$$\left.\frac{\partial S_{e,i}}{\partial D_i}\right|_{D_i = D_{c,i}} = 0. \quad (9)$$

The critical saturation ratio, $S_{c,i}$, for particle i can then be found by evaluating the equilibrium saturation ratio (8) at the critical diameter, giving

$$S_{c,i} = S_{e,i}|_{D_i = D_{c,i}}. \quad (10)$$

The critical supersaturation is then defined as

$$s_{c,i} = S_{c,i} - 1. \quad (11)$$

3. Description of Simulations

[23] The simulations in this paper were performed in a two-stage process. First, we simulated a single Lagrangian parcel moving over a polluted urban environment for 48 h, which we call *plume time* t_p (see Section 4.1). Second, we took snapshots of the aerosol population at each hour (giving 49 snapshots in total) and used these as input for 49 separate cloud parcel simulations, each lasting for 10 min of *cloud parcel time* t_c (see Section 5). The cloud parcel simulations thus do not feed back into the urban plume simulation. Instead, they are used to accurately compute and compare the process of cloud droplet formation and growth for underlying aerosol populations that have experienced different degrees of aging.

[24] The urban plume simulation includes a number of aerosol processes that are treated stochastically, i.e. the dilution, emission, and Brownian coagulation of aerosol particles. To obtain statistically robust results we produced an ensemble of urban plume simulations with subsequent (strictly deterministic) cloud parcel simulations and averaged the results over the ensemble. Based on the 95% confidence intervals we concluded that an ensemble with 10 members is large enough in the case presented here. The figures in the result sections show the 10-member ensemble averages along with the 95% confidence intervals unless stated otherwise.

4. Urban Plume Simulation

4.1. Urban Plume Simulation Setup

[25] For this study we use the urban plume case as described in *Zaveri et al.* [2010], which simulates an aerosol population undergoing emissions, dilution, Brownian coagulation, and gas and aerosol chemistry for 48 h of plume time, t_p. See *Zaveri et al.* [2010] for a detailed analysis of these simulation results. Here we summarize this simulation as it pertains to the discussion of the cloud parcel results. The simulation was run with approximately N_p = 10000 simulated particles, with the exact number of particles varying over the course of the simulated period. The time step for the urban plume simulations was 60 s.

[26] For this scenario we assumed that an air parcel containing background air was advected within the mixed layer across a large urban area. While traveling over the urban area in the first 12 h, the air parcel was exposed to continuous emissions of NO_x, SO_2, CO, volatile organic compounds (VOCs), and primary aerosol particles of three different types, namely diesel soot (70% black carbon (BC) + 30% primary organic aerosol (POA)), gasoline soot (20% BC + 80% POA), and meat cooking primary organic aerosol (100% POA). Table 1 lists the details for the initial and emitted aerosol size distribution parameters.

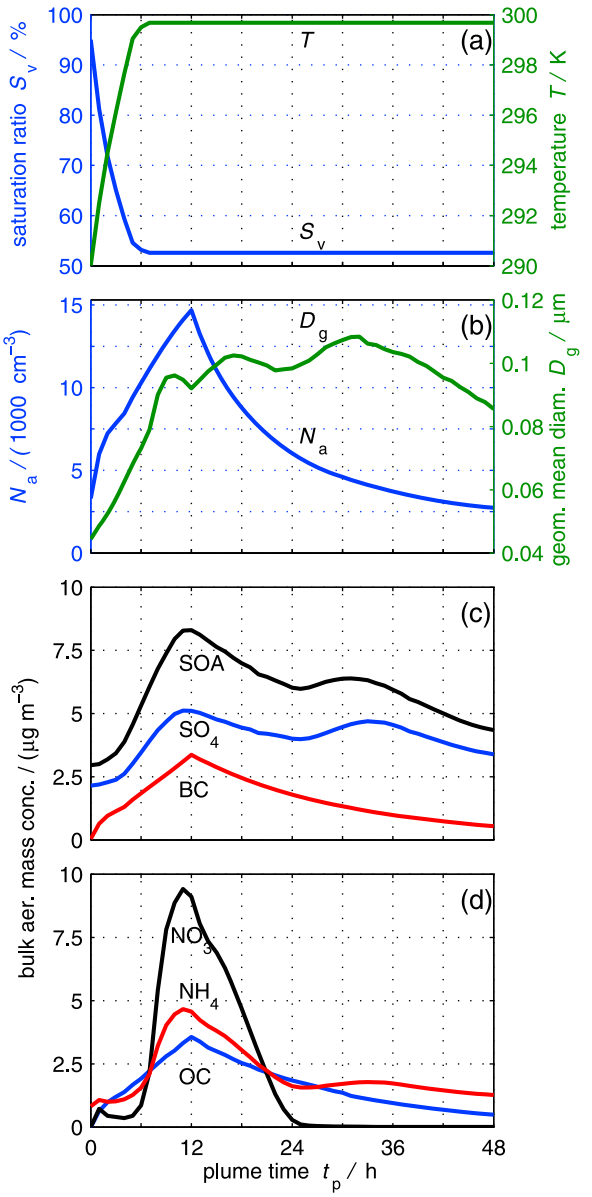

Figure 1. (a) Prescribed temperature T and calculated saturation ratio S_v over the course of the two-day urban plume simulation, (b) evolution of total particle number concentration N_a and geometric mean diameter of the dry aerosol particle population D_g, and (c and d) evolution of key bulk aerosol species. The results from this simulation serve as input data for the cloud parcel model.

[27] While the cloud parcel simulations did not include any entrainment as described in Section 2.2, the urban plume air parcel did experience dilution due to vertical entrainment of background air during the first 6 h as the mixed layer continued to grow, and continuous dilution with background air due to horizontal dispersion. The latter was modeled as a first order process, assuming a dilution rate of 5.4% h^{-1}. The background air was composed of 50 ppbv O_3 and low concentrations of other trace gases. It also contained background aerosol consisting of ammonium sulfate and secondary organic aerosol with trace amounts of black carbon in internal mixture.

[28] The temperature was prescribed along the trajectory, as shown in Figure 1a. For simplicity we assumed that the temperature stayed constant after the first 6 h. This is consistent with the idea that the air parcel remained in the fully mature mixed layer or the residual layer thereafter. The total water content of the air was assumed to be constant along the trajectory, so the saturation ratio varied as shown in Figure 1a.

4.2. Urban Plume Simulation Results

[29] Figures 1b–1d show the evolution of the total aerosol number concentration and bulk aerosol mass concentration of the major aerosol species, respectively, in the air parcel traveling with the plume. The particle number concentration N_a increased initially due to the emission of primary particles and reached a maximum of 15 000 cm^{-3} at t_p = 12 h. After t_p = 12 h, N_a decreased because the emissions were switched off, and dilution and coagulation reduced the particle number concentration. Similarly, the BC and POA mass concentration increased for the first 12 h due to emission, and decreased thereafter due to dilution with the background. The time series of the secondary aerosol species sulfate and SOA were determined by the interplay between loss by dilution and photochemical production. The ammonium nitrate mass concentration depended on the gas concentrations of its precursors, HNO_3 and NH_3. When the two gas precursors were abundant during the first 12 h, ammonium nitrate formed rapidly. After this HNO_3 and NH_3 decreased due to dilution, and the ammonium nitrate evaporated. Figure 1b shows the geometric mean diameter of the particle population, which increased from about 50 nm to 100 nm over the course of the first day due to the condensation of secondary species.

[30] To characterize the black carbon mixing state we define the per-particle BC mass fraction in particle i as

$$w_{\mathrm{BC,dry},i} = \frac{\mu_i^{\mathrm{BC}}}{\mu_i^{\mathrm{dry}}}, \tag{12}$$

where μ_i^{BC} is the mass of BC in particle i and μ_i^{dry} is the total dry mass of the particle (non-water mass). We then define a two-dimensional number concentration that is a function of both diameter and BC mass fraction. The two-dimensional cumulative number distribution $N(D, w)$ is the number of particles per volume that have a diameter less than D and a BC mass fraction less than w. The two-dimensional number distribution $n(D, w)$ is then defined by

$$n(D, w) = \frac{\partial^2 N(D, w)}{\partial \log_{10} D \, \partial w}. \tag{13}$$

[31] Figure 2 shows the two-dimensional number concentration distribution of the particles as a function of dry diameter and BC dry mass fraction, $n(D_{\mathrm{dry}}, w_{\mathrm{BC,dry}})$, after 1, 7, 15, and 36 h of simulation. This corresponds to local standard times 0700, 1300, 2100, and 1800 on the next day.

[32] At t_p = 1 h (Figure 2a) three major types of particles could be distinguished. They corresponded to the meat cooking emissions and background particles ($w_{\mathrm{BC,dry}}$ = 0% and $w_{\mathrm{BC,dry}}$ = 0.72%, respectively), gasoline vehicle emissions ($w_{\mathrm{BC,dry}}$ = 20%), and diesel vehicle emissions ($w_{\mathrm{BC,dry}}$ = 70%). Some particles existed with intermediate values for $w_{\mathrm{BC,dry}}$.

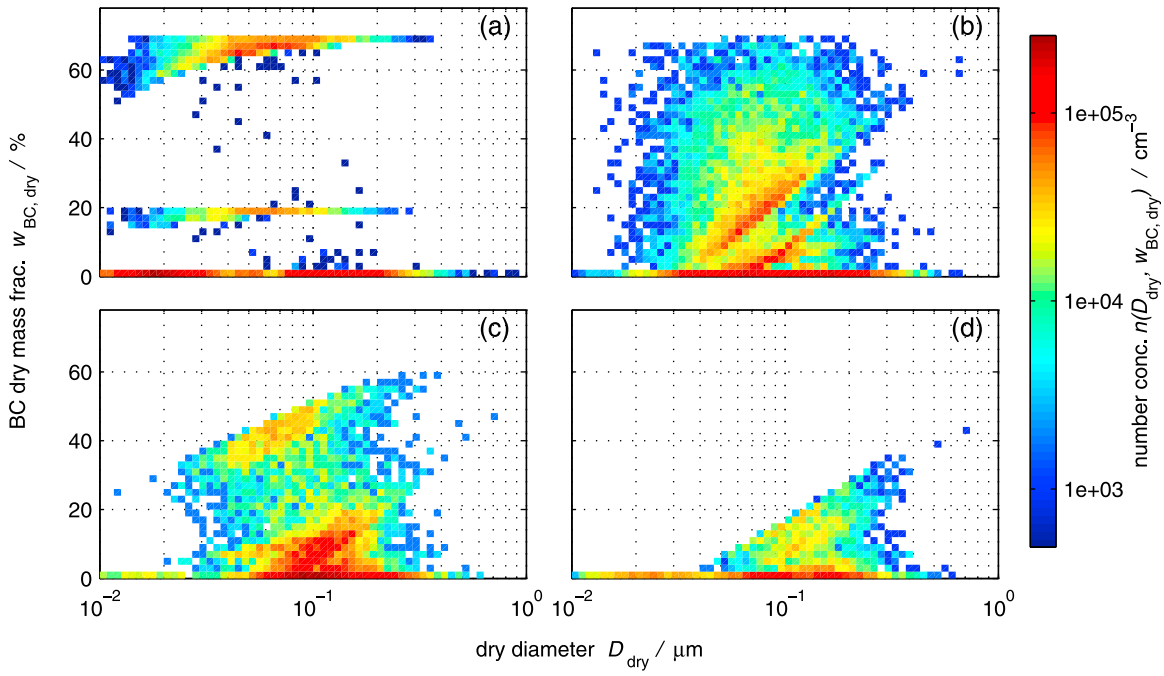

Figure 2. Two-dimensional number concentration distribution $n(D_{dry}, w_{BC,dry})$ at (a) t_p = 1 h, (b) 7 h, (c) 15 h, and (d) 36 h.

They were the result of the formation of secondary aerosol species condensing onto the particles and coagulation among particles, thereby changing $w_{BC,dry}$ over time.

[33] At t_p = 7 h (Figure 2b) a continuum of black carbon mixing states had developed as a result of continued fresh emissions on the one hand and the subsequent aging of those particles due to coagulation and condensation on the other hand. Most particles had a black carbon mass fraction between 0% and 30%. The diagonal lines appeared due to the fact that as condensation was ongoing, the BC mass fraction of small particles decreased faster than that of large particles.

[34] At t_p = 12 h emissions were switched off, and from that time onwards diesel emission particles with $w_{BC,dry}$ = 70% were no longer replenished. This is evident in the graph for t_p = 15 h (Figure 2c) where the maximum BC mass fraction had decreased to 60%. Concurrently the small BC containing particles were depleted by coagulation with larger particles. This continued for the remainder of the simulation so that at t_p = 36 h (Figure 2d) most particles had a BC mass fraction lower than 40%. The particles smaller than 0.04 μm are background particles that continued to enter the parcel by dilution. It should be noted that the mass fractions of species other than BC also changed, and hence the aerosol mixing state with respect to other species, but we do not include these figures here for brevity.

[35] Similarly to $w_{BC,dry}$ we can use the hygroscopicity parameter κ to define a two-dimensional number concentration distribution $n(D, \kappa)$. The result is shown in Figure 3, which displays the particle population at the same points in time as Figure 2. Figure 3a shows three sub-populations for t_p = 1 h. The sub-population at $\kappa \approx 0$ represents the freshly emitted BC-containing particles (diesel and gasoline) as well as the particles originating from meat cooking. The sub-population at $\kappa \approx 0.4$ consists of background particles that contained a mixture of ammonium sulfate and biogenic SOA (see Table 1). The double-banded structure can be explained by differing nitrate contents owing to the timing when the particles entered the plume and the resulting impact on water uptake and nitrate formation. Particles that were present at t_p = 0 or that were diluted in shortly after contained water because the saturation ratio S_v was above the deliquescence point (see Figure 1a). These particles were able to acquire nitrate, which raised their κ-value slightly. During the simulation S_v in the plume decreased, and particles that entered the simulation after S_v dropped below the deliquescence point, remained dry. Nitrate formation was not possible on these particles in the first few hours of simulation because the HNO_3 mixing ratio was still too low. These particles form the band at κ = 0.34. We observe a third band around $\kappa \approx 0.6$. These are background particles that lost their biogenic SOA material due to evaporation.

[36] As the aerosol particles were processed in the plume and condensation of inorganic and organic semivolatile species occurred as well as coagulation these structures changed accordingly. At t_p = 7 h a continuous range of κ values was established as very freshly emitted BC-containing particles coexisted with particles that had experienced aging of different degrees. At this plume time all particles contained some SOA, which explains why κ was less than 0.6 for all particles. After emissions stopped, particles with $\kappa \approx 0$ were not replenished anymore and the clusters of particles moved along the κ-axis to larger values. Background particles were continuously diluted in as already seen in Figure 2. Given the temperature of the air parcel and the concentration level of biogenic SOA precursor, their SOA material evaporated, and they show as a line at κ = 0.65.

[37] Figure 4 shows the two-dimensional number concentration distribution as a function of the dry diameter and critical supersaturation, $n(D_{dry}, s_c)$, at the same times as in

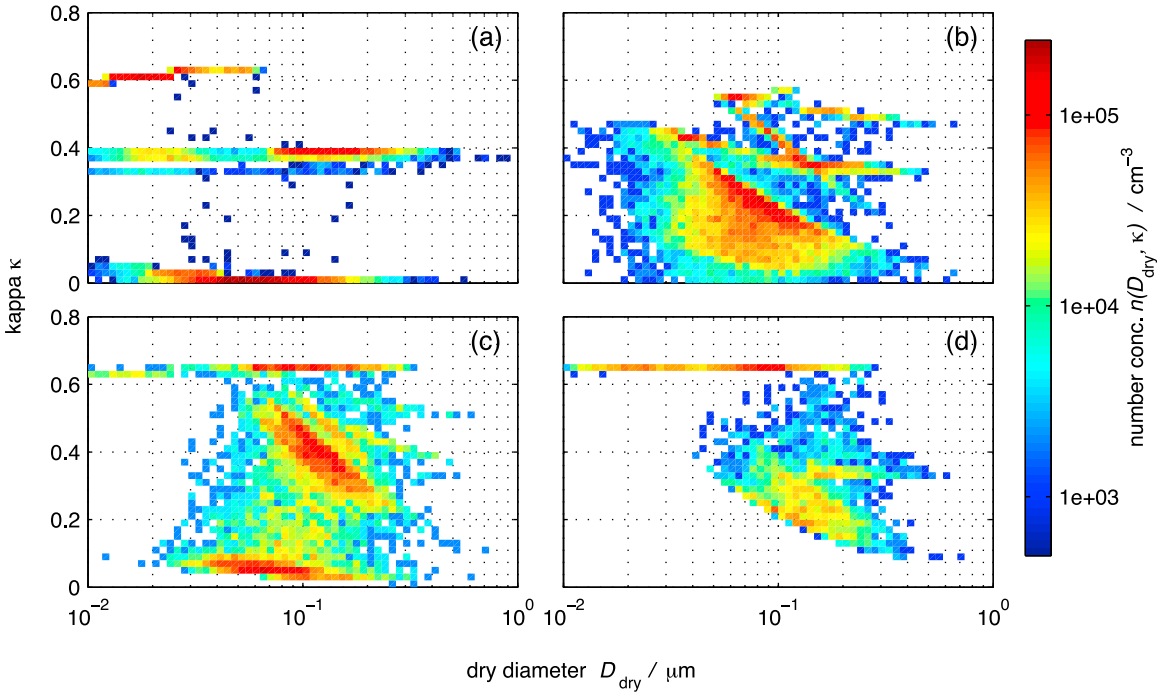

Figure 3. Two-dimensional number concentration distribution $n(D_{dry}, \kappa)$ at (a) t_p = 1 h, (b) 7 h, (c) 15 h, and (d) 36 h.

Figures 2 and 3. As expected from Köhler theory, the larger the size of the particle, the lower is the critical supersaturation. However, size is not the only parameter determining critical supersaturation. At a given size the particles can have different critical supersaturation values due to differences in their compositions. For example at t_p = 1 h, particles with size of 0.1 μm had s_c ranging from 0.1% to 2%. At t_p = 1 h, the two maxima of the 2-D distribution, $n(D_{dry}, s_c)$ corresponded to gasoline and diesel particles (low κ) and to background particles (high κ).

[38] As the simulation time proceeded, an increasing number of particles became more hygroscopic, and the

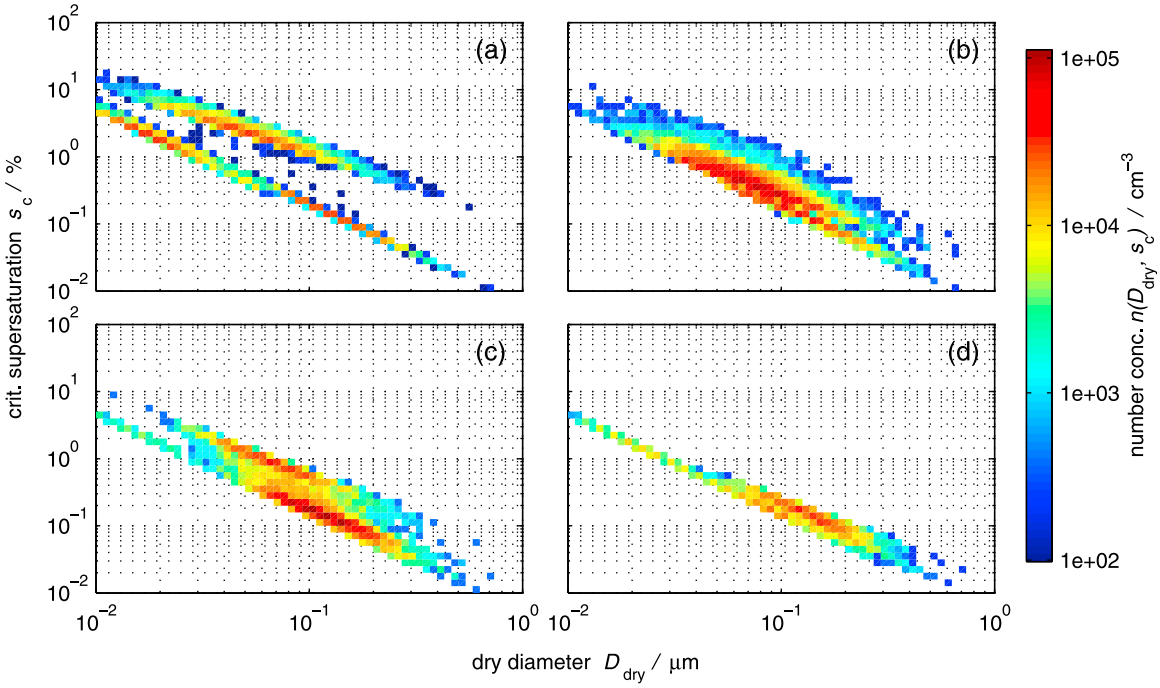

Figure 4. Two-dimensional number concentration distribution $n(D_{dry}, s_c)$, at (a) t_p = 1 h, (b) 7 h, (c) 15 h, and (d) 36 h.

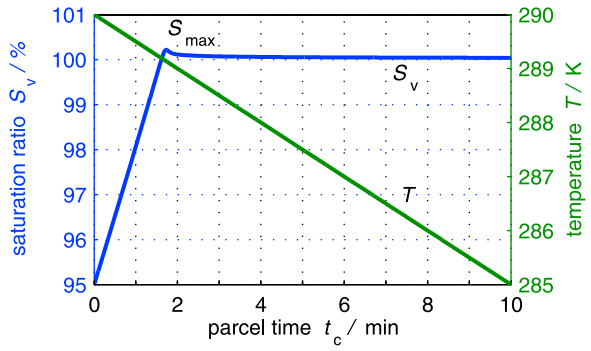

Figure 5. Evolution of temperature T and saturation ratio S_v over the course of a 10-min cloud parcel simulation. While the T-profile was prescribed, S_v was the result of cooling and water uptake by the aerosol population growing into cloud droplets. For this specific example we used the particle population at t_p = 15 h as initial condition. S_{max} labels the maximum saturation ratio S_v reached during the cloud parcel simulation.

maximum of the number concentration distribution moved to lower s_c values. However, since during the emission phase fresh emissions were continuously supplied, the spread of the distribution with respect to s_c was maintained. Only after emissions were turned off, the distribution with respect to s_c became narrower meaning that the aerosol distribution moved toward an "internally mixed" state with respect to CCN properties. This is apparent in the graph for t_p = 36 h.

[39] Figure 4 is consistent with the findings by *Dusek et al.* [2006], often loosely paraphrased as "size matters more than composition". It shows that resolving size is imperative for predicting CCN properties as it is the dominant factor in determining critical supersaturation. Differences in composition modulate this relationship by causing some spread of $n(D_{dry}, s_c)$ in the s_c-dimension. This spread tends to be large when particles of very different hygroscopic properties are present. There are various circumstances that can lead to such conditions. In our simulations this is the case at early plume times, when background particles coexist with freshly emitted BC-containing particles. Further, this spread is also maintained when fresh emissions enter the air parcel, and at the same time efficient aging mechanisms are operating, as occurs during the daytime in our simulations. When emissions stop, but aging mechanisms are still at work, the aerosol population moves toward an internal mixture with respect to CCN properties, and consequently the spread in s_c-dimension becomes smaller, as can be seen on the second day of our simulations.

5. Cloud Parcel Simulation

5.1. Cloud Parcel Simulation Setup

[40] Each cloud parcel simulation was initialized with the aerosol population taken from a specific point along the urban plume trajectory, corresponding to a particular plume time, t_p. The cloud parcel model simulations started at a saturation ratio of S_v = 95% and a temperature of T = 290 K, and the particle population had the initial per-particle water content v_i^w adjusted so that each particle was at equilibrium (i.e., so that $S_{e,i}$ = 95% in (8)). The time step for the cloud parcel simulations was 1 second.

[41] For the base case the cloud parcel model was then run for 10 min of cloud parcel time, t_c, with a constant temperature decrease of 0.5 K/min prescribed throughout the 10 min simulation and constant pressure. This cooling rate can be approximately interpreted as modeling an air parcel with an updraft velocity on the order of 0.85 m/s (assuming subsaturated, double this velocity for supersaturated). Since previous studies showed a profound impact of the cooling rate on CDNC [*Feingold*, 2003], we performed two additional sets of cloud parcel simulations, one set with a cooling rate of 0.25 K/min and one set with 1 K/min.

5.2. Cloud Parcel Simulation Results

[42] We used the particle-resolved aerosol population output from the urban plume simulation at every hour as input to the cloud parcel model as described in Section 2.2. As shown in Figures 1 and 2 these particle populations represented urban, polluted conditions where the bulk concentrations as well as the mixing state varied from hour to hour.

[43] Figure 5 shows an example for the time series of temperature and saturation ratio as a function of cloud parcel time t_c. Here we used the aerosol distribution at plume time t_p = 15 h as input and the cooling rate of 0.5 K/min. The evolution of the saturation ratio was the result of the interplay of the prescribed cooling rate and the loss of water vapor due to condensation on the particles according to equation (7). In this example a maximum saturation ratio of S_{max} = 100.22% was reached at t_c = 1.75 min.

[44] Figure 6 shows the corresponding particle and droplet number size distribution as a function of wet diameter, $n(D_{wet})$, at t_c = 0 min (red), 2 min (blue), 10 min (green). The spectrum at t_c = 0 min is the aerosol distribution at t_p = 15 h. At t_c = 2 min, aerosol activation had occurred and the spectrum had become bimodal. The mode with the larger particles represents the cloud droplets with a mean wet diameter of $\bar{D}$ = 3.8 μm and a relative dispersion of ϵ = 0.19. Relative dispersion is defined as the ratio of the standard

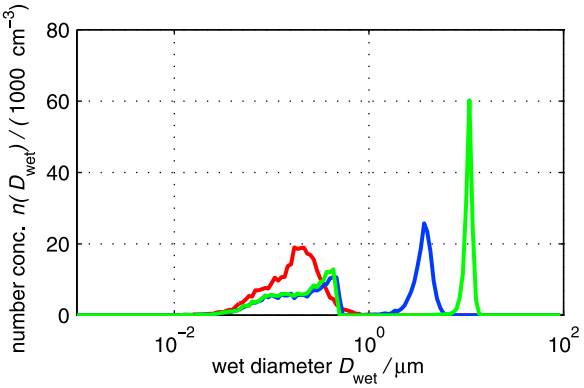

Figure 6. Size distributions based on wet diameter $n(D_{wet})$ at t_c = 0 min (red), 2 min (blue) and 10 min (green). We used the particle population at t_p = 15 h as initial condition.

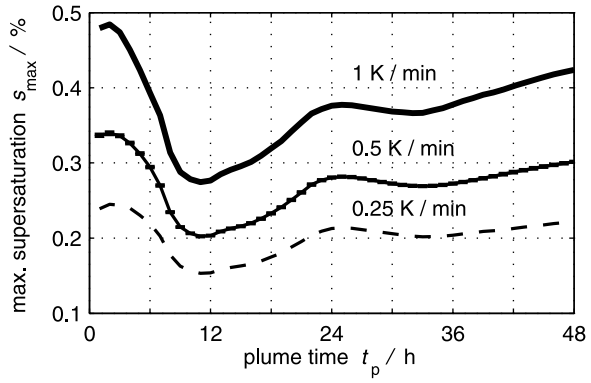

Figure 7. Maximum supersaturation, s_{max}, attained in the 10-min parcel simulations as a function of plume time t_p. The thin solid line (cooling rate of 0.5 K/min) shows the average of an ensemble of 10 simulations. The error bars represent the 95% confidence interval. The thick solid line (cooling rate of 1 K/min) and the dashed line (cooling rate of 0.25 K/min) represent one ensemble member.

deviation of the size spectrum $\sigma(n(D))$ to the mean diameter $\bar{D}$, so that

$$\epsilon = \frac{\sigma(n(D))}{\bar{D}}. \quad (14)$$

The mode with the smaller particles represents the interstitial aerosol. As the environmental relative humidity increased at the start of the simulation, these particles exhibited hygroscopic growth.

[45] At t_c = 10 min, the interstitial population remained essentially unchanged compared to t_c = 2 min, while the cloud droplet distribution had further grown to a mean diameter of $\bar{D} = 10.9\,\mu$m. The cloud droplet mode had also narrowed to $\epsilon = 0.10$. Note that the particle-resolved method does not suffer from numerical diffusion when calculating the rapid growth of the activated cloud droplets.

[46] In this study we followed *Cubison et al.* [2008] and counted the particles that resided in the mode with larger sizes (i.e. $D_{wet} > 2\ \mu$m) as cloud droplets. It is possible that amongst this droplet mode there were some particles that had a critical diameter larger than 2 μm and that this critical diameter was not reached during the simulation time. Those particles, although of similar sizes as the activated cloud drops, were then not yet activated. This "inertial effect" was described by *Chuang et al.* [1997] and *Nenes et al.* [2001]. As detailed analysis of our model output revealed, most of the particles with critical diameter larger than 2 μm were indeed activated cloud droplets, i.e. they exceeded their critical diameters during the simulation time and continued to grow until the end of the simulation. Only very few of the droplets in our cloud parcel simulations were subject to the inertial effect.

[47] In Figure 7 we mapped the resulting maximum supersaturations s_{max} for the three sets of cloud parcel runs as a function of plume time t_p. For each set we used the same temperature profile for all cloud parcels, therefore the exact value for s_{max} depended exclusively on the initial aerosol distribution. It ranged for the base case between 0.35% for cloud parcels that were initialized with the aerosol population at t_p = 0 h and 0.2% for cloud parcels that were initialized with aerosol populations around t_p = 12 h. As expected, low values of s_{max} were reached when the cloud parcel simulations were initialized with aerosol populations that contained a large number of aerosol particles and that were able to activate to cloud droplets competing for water vapor.

[48] For further analysis, we define the cloud droplet fraction, f_N, as the ratio of cloud droplet number concentration, N_d, to the total number concentration of particles, N_a. The nucleation-scavenged mass concentration of BC is defined as the mass concentration of BC associated with the cloud droplets. The nucleation-scavenged mass fraction of BC, f_{BC}, is then defined as the ratio of BC mass concentration that is associated with the cloud droplets to the total BC mass concentration.

[49] Figure 8 shows the results of f_N and f_{BC} for the 49 cloud parcel simulations. The fraction of particles that became cloud droplets generally increased for cloud parcels initialized with particle populations from the later part of the 48-hour urban plume simulation. While during the morning of the first day f_N amounted to only 20%, this increased to about 70% by the end of the second day. This is consistent

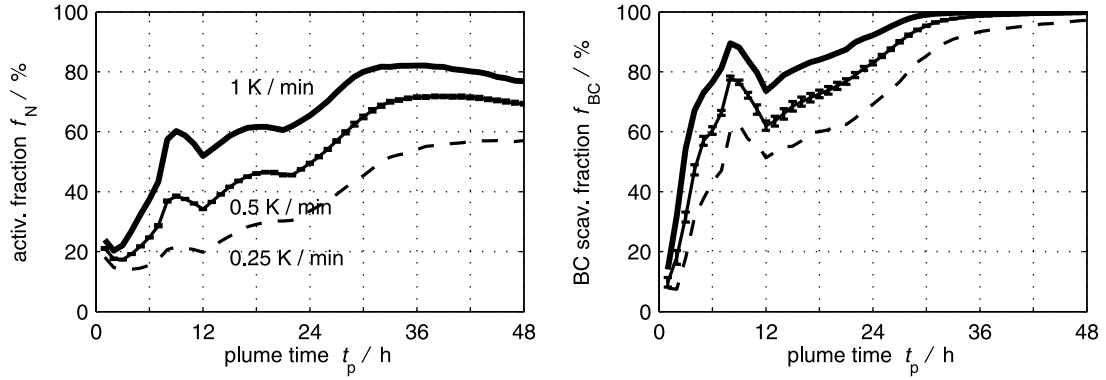

Figure 8. The same as Figure 7, but for (a) cloud droplet number fraction f_N, and (b) nucleation-scavenged BC mass fraction f_{BC} as a function of plume time t_p.

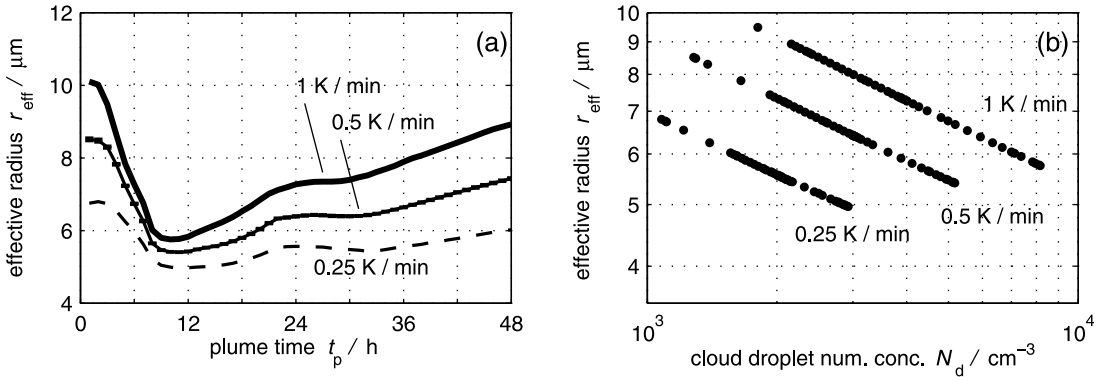

Figure 9. (a) The same as Figure 7, but for effective radius r_{eff} at t_c = 10 min as a function of plume time t_p. (b) Relationship between the total cloud droplet number concentration N_d and the effective radius r_{eff}.

with the notion that the aerosol population during the early plume hours contained a large proportion of "fresh" BC containing particles, which were not easily activated. Over the course of the simulation these particles "aged", hence f_N increased.

[50] Similar arguments apply to f_{BC}. One hour after the simulation started, only 10% of the BC mass concentration was contained in the activated cloud droplets. This value increased quickly during the next 7 hours until f_{BC} was about 80% at t_p = 8 h. For cloud parcels from t_p = 40 h onwards almost 100% of the BC mass concentration was incorporated in the cloud droplets. Note that the dependence of f_N and f_{BC} on plume time t_p is the result of the interplay of the numerators' and denominators' magnitudes, and that both the total aerosol number concentration N_a and the total BC mass concentration display a very pronounced characteristic temporal profile shown in Figures 1b and 1d for reasons discussed in Section 4.2.

[51] However, the aging process was not necessarily monotone. For the cloud parcels between t_p = 9 h and t_p = 12 h f_N and f_{BC} decreased before increasing again. This behavior was caused by the timing of the emissions and the production of condensable hygroscopic material. Emissions of diesel and gasoline particles were ongoing until t_p = 12 h (1800 LST). The particles emitted in the late afternoon did not age as quickly as the ones in the late morning, since photochemistry had slowed down by that time, hence the decrease in f_N and f_{BC}. These quantities started increasing again after emissions had stopped. Further process analysis revealed that both condensation and coagulation contributed to the aging process in this urban plume scenario. However, the relative importance of the two aging mechanisms depended on the time of the day. During the day condensation was the dominant aging process, since condensable secondary aerosol mass was readily produced by photochemistry. During the night these processes ceased and coagulation of BC-containing particles with large, hygroscopic background particles became more important [*Riemer et al.*, 2010].

[52] Figure 9a shows the effective radius r_{eff} of the cloud droplet mode at t_c = 10 min as a function of t_p. The effective radius is important for cloud radiative transfer and remote sensing calculations [*Brenguier et al.*, 2000; *Liu and Daum*, 2002; *Feingold et al.*, 2003; *Feingold*, 2003; *Twohy et al.*, 2005] and defined as the ratio of the third moment to the second moment of the cloud droplet size number distribution:

$$r_{\mathrm{eff}} = \frac{\int_{r_{\min}}^{\infty} r^3 n(r)\,dr}{\int_{r_{\min}}^{\infty} r^2 n(r)\,dr}, \tag{15}$$

where the r_{min} equals 1 μm and $n(r)$ is the number size distribution in terms of wet radius, r, of the particles. For the different cloud parcel simulations of the base case r_{eff} ranged between 5.5 μm and 8.5 μm. The lowest values were obtained for the cloud parcels initialized with aerosol populations around t_p = 11 h. These were the parcels with the highest aerosol number concentrations (cf. Figure 1) and also the highest cloud droplet number concentration, consistent with the first indirect effect [*Twomey*, 1974] given that the liquid water content is the same for each cloud parcel. Figure 9b shows r_{eff} versus the corresponding cloud droplet concentration N_d and shows the relationship of $r_{eff} \sim N_d^{-1/3}$. This relationship is expected for adiabatic conditions

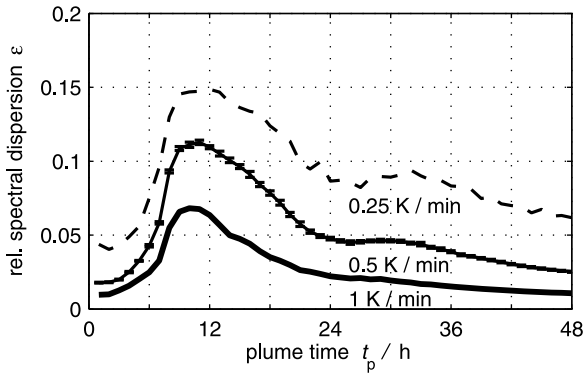

Figure 10. The same as Figure 7, but for relative spectral dispersion of the cloud droplet size spectra ϵ at t_c = 10 min as a function of plume time t_p.

[*McFarquhar and Heymsfield*, 2001], but in reality the exponent can deviate significantly from −1/3 [*McComiskey et al.*, 2009].

[53] Figure 10 displays the relative spectral dispersion ϵ of the cloud droplet mode at t_c = 10 min as a function of t_p. The dispersion of the cloud droplet spectrum is of interest for cloud parameterization schemes related to warm rain processes and auto-conversion rates [*Liu and Daum*, 2000; *Rotstayn and Liu*, 2003] and for parameterizing the effective radius of cloud droplets in global climate models [*Liu and Daum*, 2002; *Peng et al.*, 2002].

[54] The values range between 0.017 and 0.11, with the largest values occurring for the cloud parcels initialized with aerosol distributions around t_p = 11 h, coinciding with the cloud parcel with the smallest effective radius and largest cloud droplet number concentrations. This is consistent with *Liu and Daum* [2002] who conclude from field data that polluted clouds are associated with larger relative dispersion.

5.3. Impact of Cooling Rate on the Reference Case

[55] In addition to the base case that used a cooling rate of 0.5 K/min, Figures 7–10 include the results of two additional simulations with a cooling rate of 0.25 K/min and 1 K/min, respectively. The results show the expected behavior. A higher cooling rate lead to higher supersaturation values (Figure 7). While the base case values ranged between 0.2% and 0.34%, the cooling rate of 1 K/min resulted in a range of 0.28% and 0.49%, and the cooling rate of 0.25 K/min yielded a range of 0.16% to 0.25%. The qualitative dependence on plume time is the same for the three cooling rates with the lowest supersaturation values obtained during the plume times with the largest abundance of aerosol particles.

[56] Figure 8 shows that a higher cooling rate generally lead to larger values of f_N and f_{BC}. For example on the second day of simulation the cooling rate of 1 K/min yielded f_N of 80% whereas the cooling rate of 0.25 K/min plateaued at 58%. However, the differences in f_N and f_{BC} for at early plume hours are relatively small. This can be explained by the fact that these aerosol populations contained fresh emissions, which were not accessible for activation for the supersaturations produced by either of the three cooling rates. This can also be seen in Figure 4a, which shows that the maximum of the number concentration distribution $n(D_{dry}, s_c)$ for the upper branch representing the fresh emissions lies mostly above a supersaturation of 1%.

[57] Figure 9 shows that with a higher cooling rate a higher effective radius was reached. The range with respect to plume time was enhanced when the cooling rate was higher, between 6 μm and 10 μm for 1 K/min versus 5 μm and 7 μm for 0.25 K/min. The relative dispersion shows the opposite behavior, with the largest values attained for the lowest cooling rate as evident in Figure 10.

6. Quantifying the Importance of Mixing State

[58] We will now turn to the question of how important it is to know the mixing state for understanding aerosol activation and the nucleation-scavenging of BC. To answer this question, we took the following approach: In addition to the reference case (scenario "ref"), where we used particle-resolved model results as input for the cloud parcel model, we performed three different averaging procedures on the particle-resolved data before using them as parcel model input. Specifically we distinguish between composition averaging (scenario "comp"), size-bin averaging (scenario "size"), and averaging of both composition and size (scenario "both"). All three averaging scenarios were implemented by binning the particle-resolved aerosol population ("ref") into 20 logarithmically spaced size bins from 1 nm to 10 μm. The number of particles in each bin remained unchanged by the averaging procedures.

[59] For the scenario "comp" we assigned the bin-averaged composition to all particles within one size bin. The particle sizes remained unchanged. For the scenario "size" we assigned the bin-averaged particle volume to all particles within each size bin while preserving their per-particle species ratios. For the scenario "both" we applied composition averaging first, and then size-bin averaging. The resulting size distribution corresponds to a traditional moving-center sectional method [*Jacobson*, 1997]. The detailed description of each procedure and their properties is given in Appendix B.

6.1. Averaged Simulation Results

[60] The purpose of the composition- and the size-bin-averaging scenario is to separate out the importance of composition resolution versus size resolution. Figures 11, 12 and 13 show for one member of the ensemble how the various averaging scenarios impacted the two-dimensional particle number concentration distributions $n(D_{dry}, w_{BC,dry})$, $n(D_{dry}, \kappa)$, and $n(D_{dry}, s_c)$. In the "comp" scenario, the particles in one size bin retained their original sizes, but their compositions were averaged as shown in Figure 11b. The corresponding $n(D_{dry}, \kappa)$ distribution (Figure 12b) does not have the spread in κ-dimension as the reference case does. Instead of covering a wide range of κ values between near-zero and 0.65 the particles are mapped to a mean value of kappa of about 0.4 for large parts of the size spectrum. Likewise, the corresponding $n(D_{dry}, s_c)$ distribution does not have the spread in s_c direction as the reference case does.

[61] Since the "size" scenario forced particles in one bin to have the same size while they can have different compositions, the two-dimensional distributions appear as a number of vertical lines (Figures 11c, 12c and 13c). In the "both" scenario, the size-bin averaging was done after composition averaging, thus all particles had the same sizes and compositions and the two-dimensional particle number distributions were reduced to one point per size bin, as shown in Figures 11d, 12d and 13d.

[62] Using these modified initial conditions, we compared the maximum supersaturation s_{max} attained during the 10-min parcel time, the cloud droplet fraction f_N, the nucleation-scavenged fraction f_{BC}, the effective radius r_{eff}, and the relative spectral dispersion ϵ. The four latter quantities are reported at t_c = 10 min. We used the reference case as a benchmark for comparison to the three averaging schemes. Any differences can be attributed to the differences in the representations of the size and composition of the aerosol particles. Figures 14–16 show the results for the base-case cooling rate of 0.5 K/min. We will summarize the impact of a different cooling rate value at the end of this section.

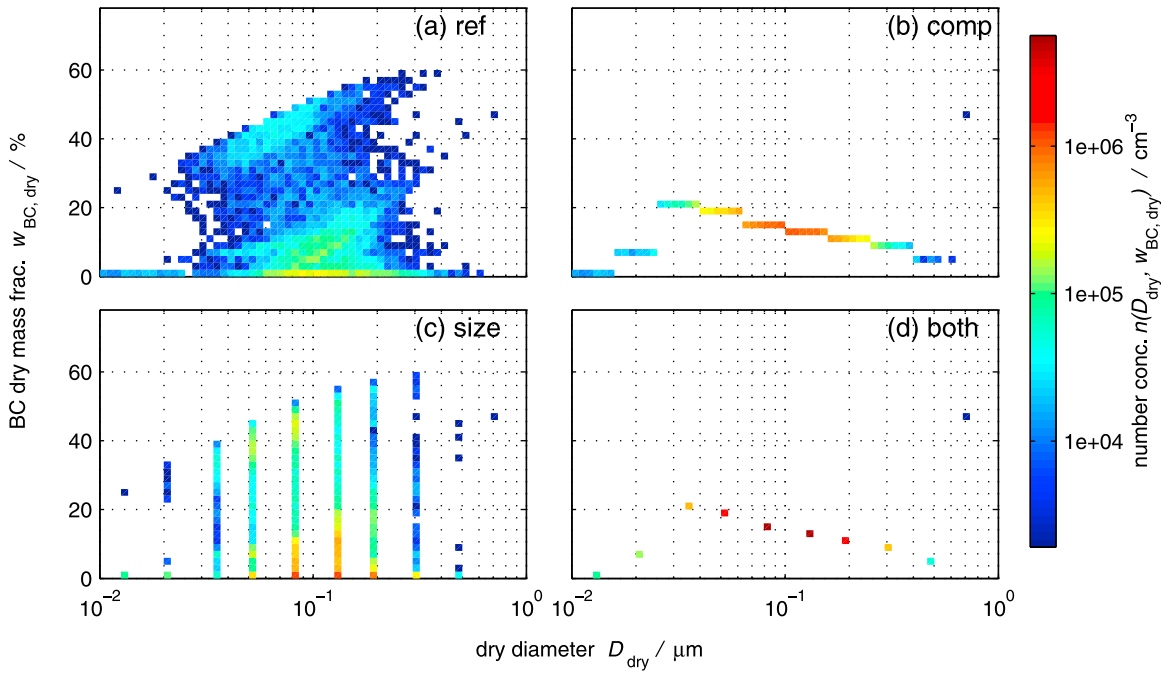

Figure 11. Two-dimensional number concentration distribution $n(D_{dry}, w_{BC,dry})$, at t_p = 15 h for scenarios (a) "ref", (b) "comp", (c) "size", and (d) "both". The results of only one member of the ensemble are shown.

[63] Figure 14 compares the attained maximum supersaturation s_{max} for the individual averaging scenarios to the reference case. The results are very close to each other, indicating that the impact of mixing state on the maximum saturation ratio is small under the conditions investigated here and that the number concentration of aerosol particles is the main driver for s_{max}. The largest (absolute) difference was Δs_{max} = 0.017% and occurred for scenario "both" at

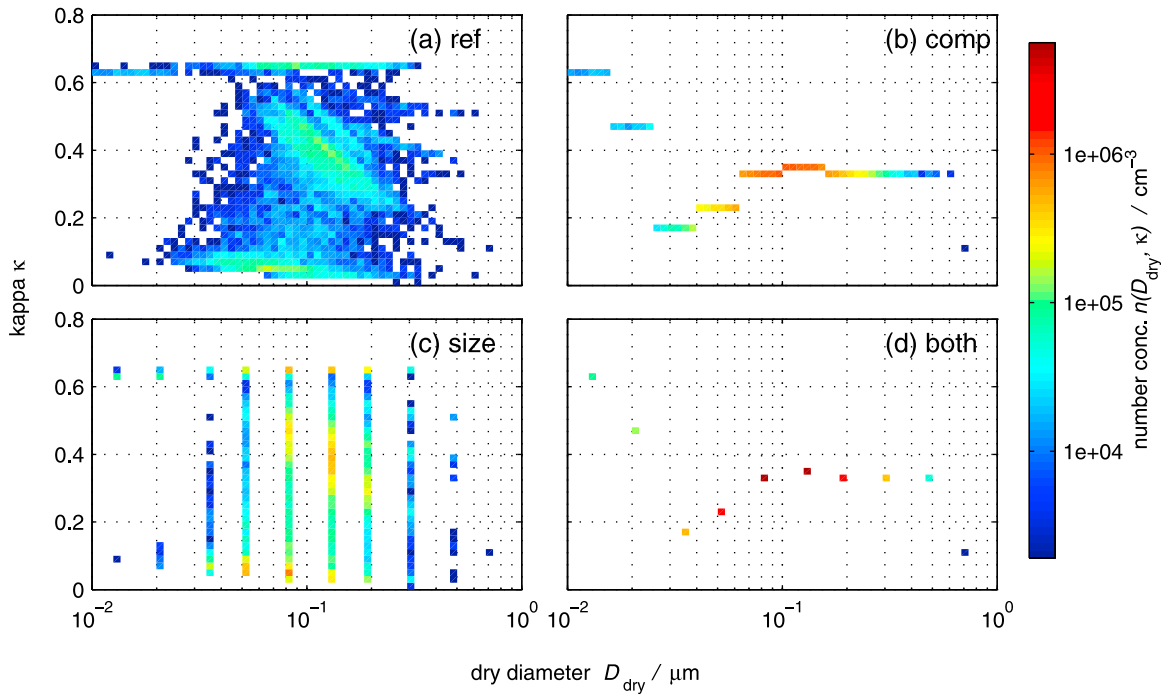

Figure 12. Two-dimensional number concentration distribution $n(D_{dry}, \kappa)$, at t_p = 15 h for scenarios (a) "ref", (b) "comp", (c) "size", and (d) "both". The results of only one member of the ensemble are shown.

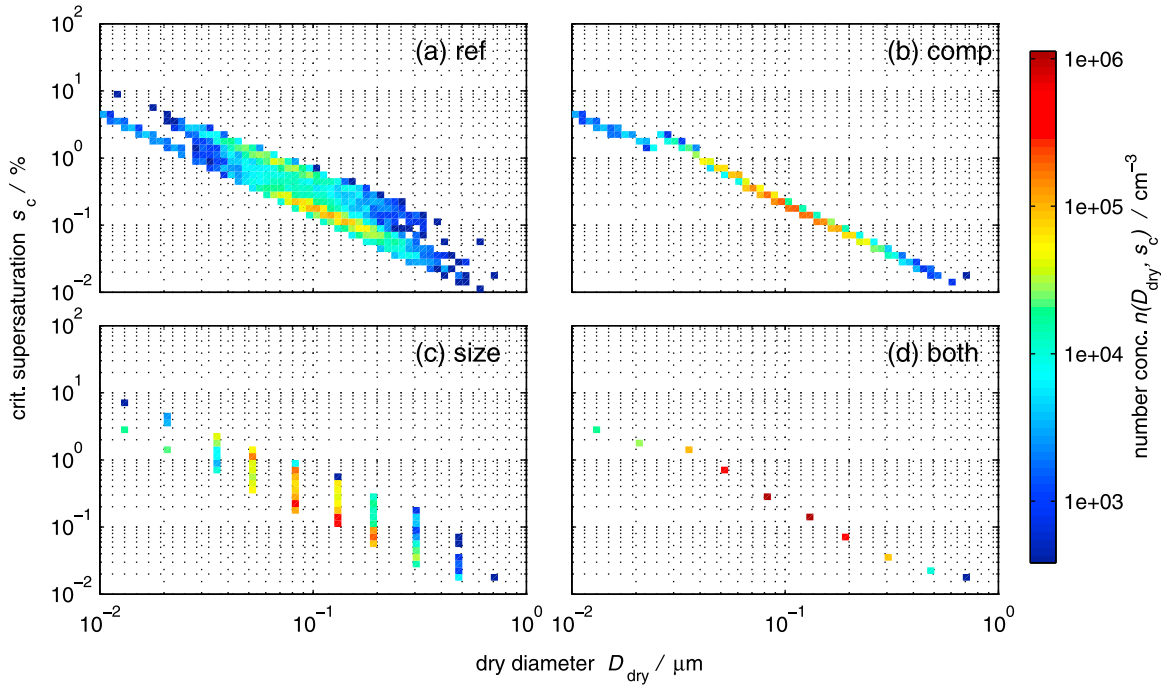

Figure 13. Two-dimensional number concentration distribution $n(D_{\mathrm{dry}}, s_c)$, at t_p = 15 h for scenarios (a) "ref", (b) "comp", (c) "size", and (d) "both". The results of only one member of the ensemble are shown.

t_p = 3 h. At that time the reference case shows a largely externally mixed particle population (similar to Figure 2a).

[64] Figure 15 shows f_N, f_{BC}, r_{eff} and ϵ as a function of t_p for the four scenarios. We give the range of relative errors for all 48 cloud parcel simulations in Table 2. For the cloud droplet fraction f_N shown in Figure 15a, composition averaging and size-bin averaging lead to relatively small errors (−3% to 25% for scenario "comp" and −2% to 11% for scenario "size"). Larger errors (−10 to 35%) arose for scenario "both", where we averaged both size and composition. Since for this case the particles in one size bin were assigned the same size and composition, all the particles in that bin simultaneously either activated or did not activate. This caused the sudden jump in f_N at t_p = 35 h, and from further investigations we concluded that this behavior is sensitive to the imposed bin positions.

[65] Figure 15b shows f_{BC} as a function of t_p. The scenario "size" follows the reference case closely with differences ranging from −15% to +5%. The "comp" and the "both" scenarios always overestimate f_{BC}, with overestimations up to 600%. Note that the stochastic variability of the model results indicated as error bars by the 95%-confidence interval is very small, so that the differences found here are indeed due to the different treatment of aerosol mixing state. For t_p = 30 h onwards the differences between the four scenarios become very small and f_{BC} reaches 100%. The reasons for the relatively large errors seen for f_{BC} in Figure 15b compared to the small errors for f_N will be further discussed below.

[66] Figures 15c and 15d show r_{eff} and ϵ as a function of t_p. The "size" and "comp" scenarios result in values very close to the reference case. Scenario "both" results in larger differences, within −9% to +4% for r_{eff} and from −47% to +50% for ϵ.

[67] The magnitude of the errors in r_{eff} amount approximately to 1/3 of the errors in f_N [*Kristjansson*, 2002]. This can be shown by writing r_{eff} as [*Rotstayn and Liu*, 2003]:

$$r_{\mathrm{eff}} = \frac{(1+2\epsilon^2)^{\frac{2}{3}}}{(1+\epsilon^2)^{\frac{1}{3}}} \left(\frac{3L}{4\pi\rho_w}\right) N_d^{-\frac{1}{3}}, \tag{16}$$

where L is the liquid water content. Given that L is constant and that the value for ϵ is smaller than 0.1, error propagation yields an approximation for the relative error in r_{eff}:

$$\frac{|\Delta r_{\mathrm{eff}}|}{r_{\mathrm{eff}}} \lesssim 2\epsilon^2 \frac{|\Delta\epsilon|}{\epsilon} + \frac{1}{3}\frac{|\Delta N_d|}{N_d} \approx \frac{1}{3}\frac{|\Delta N_d|}{N_d}, \tag{17}$$

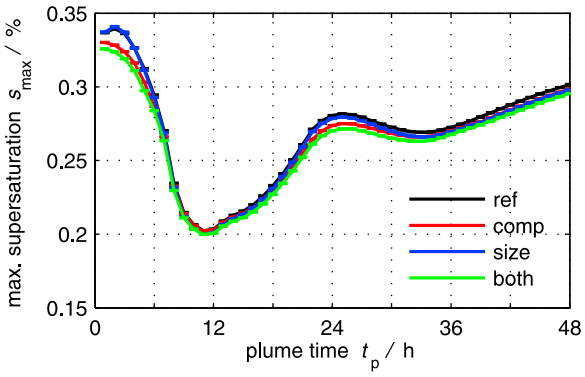

Figure 14. Maximum supersaturation, s_{max}, attained in the 10-minute parcel simulations using the base-case cooling rate of 0.5 K/min as a function of plume time t_p for the reference case and the averaging scenarios. The figure shows the average of an ensemble of 10 simulations.

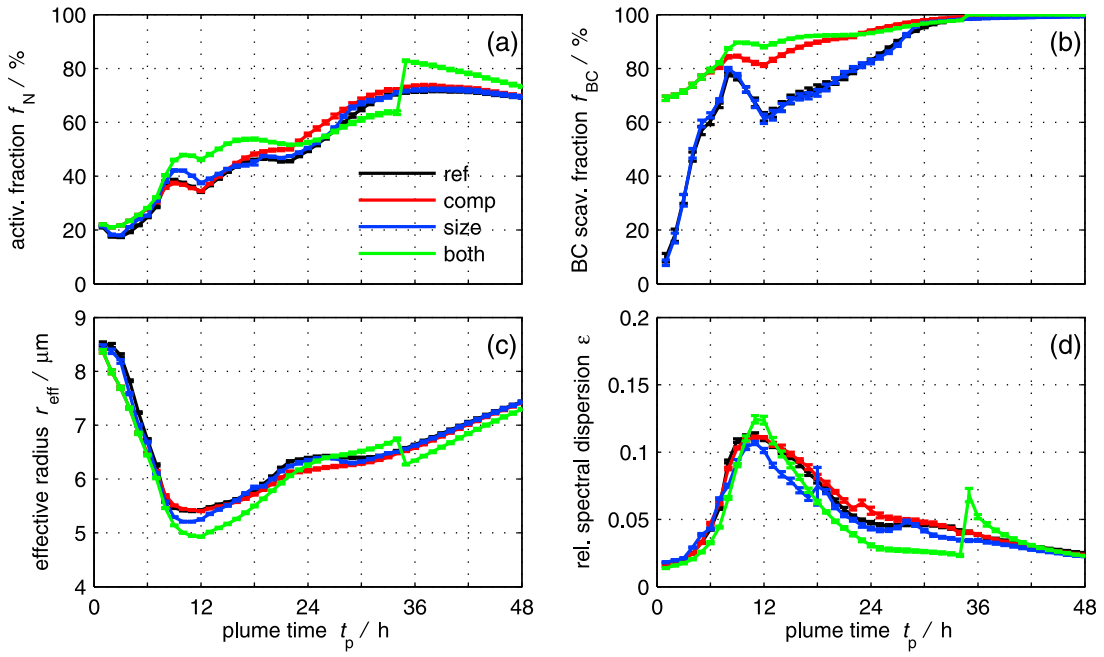

Figure 15. (a) Cloud droplet number fraction f_N, (b) nucleation-scavenged BC mass fraction, f_{BC}, (c) effective radius, r_{eff}, and (d) the relative spectral dispersion, ϵ for the reference case and averaging scenarios using the base-case cooling rate of 0.5 K/min. Each figure shows the average of an ensemble of 10 simulations.

where the final approximation is assuming that $|\Delta\epsilon|/\epsilon$ is of a similar magnitude as $|\Delta N_d|/N_d$.

[68] The order of magnitude of errors in cloud optical properties as a result of errors in r_{eff} can be estimated as follows: The maximum error for r_{eff} occurs for scenario "both" at t_p = 12 h and represents an underprediction of r_{eff} of about 10%. Assuming constant cloud thickness and cloud liquid water content, the optical depth τ is inversely

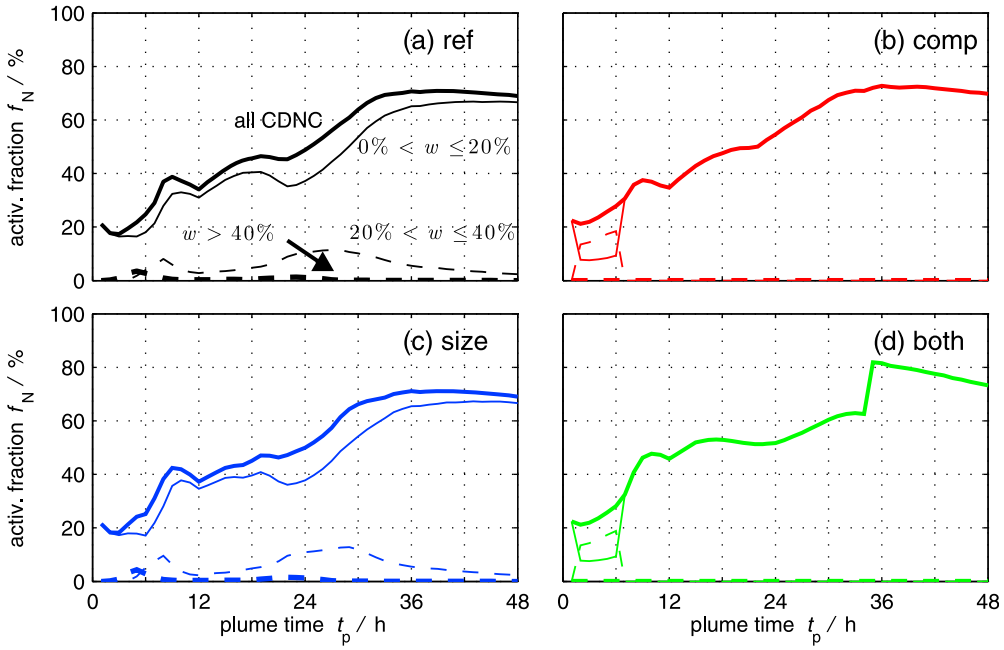

Figure 16. Cloud droplet number fraction f_N segregated according to the BC dry mass fraction $w_{BC,dry}$ of the underlying aerosol population: (a) the scenario "ref", (b) scenario "comp", (c) scenario "size" and (d) scenario "both". The thick solid line represents the total cloud droplet number fraction. The thin solid, thin dashed and thick dashed lines depict the cloud droplet number fraction with $0\% < w_{BC,dry} \leq 20\%$, $20\% < w_{BC,dry} \leq 40\%$, and $w_{BC,dry} > 40\%$, respectively.

Table 2. Relative Error Ranges for Four Physical Quantities (f_N, f_{BC}, r_{eff}, ϵ) When Computed From the Three Different Averaging Schemes ("comp", "size", "both") and Compared to the Fully Particle-Resolved Results ("ref")[a]

	"comp"	"size"	"both"
Activation fraction f_N			
$\dot{T} = -0.25$ K/min	−3.0% to +24%	−15% to +17%	−38% to +85%
$\dot{T} = -0.50$ K/min	−3.1% to +24%	−2.2% to +11%	−10% to +34%
$\dot{T} = -1.0$ K/min	+0.12% to +31%	−2.4% to +9.3%	−26% to +65%
BC scavenging fraction f_{BC}			
$\dot{T} = -0.25$ K/min	+2.0% to +790%	−12% to +20%	−7.2% to +840%
$\dot{T} = -0.50$ K/min	+0.28% to +610%	−19% to +6.7%	−0.37% to +610%
$\dot{T} = -1.0$ K/min	+0.020% to +490%	−4.0% to +6.7%	+0.0% to +550%
Effective radius r_{eff}			
$\dot{T} = -0.25$ K/min	−6.7% to +0.93%	−4.5% to +5.1%	−17% to +16%
$\dot{T} = -0.50$ K/min	−6.8% to +1.0%	−3.5% to +0.50%	−8.8% to +3.6%
$\dot{T} = -1.0$ K/min	−8.7% to −0.040%	−2.7% to +0.81%	−15% to +10%
Dispersion ϵ			
$\dot{T} = -0.25$ K/min	−9.3% to +32%	−33% to +120%	−73% to +420%
$\dot{T} = -0.50$ K/min	−15% to +18%	−24% to +19%	−47% to +50%
$\dot{T} = -1.0$ K/min	−4.6% to +43%	−13% to +36%	−59% to +340%

[a]The relative error ranges are for one representative of the ten members in the ensemble and give the smallest and largest errors (negative values are under-predictions, positive values are over-predictions) observed from $t_p = 1$ h to $t_p = 48$ h (i.e., excluding the first hour of simulation). The minimum and maximum values of the error for any given physical quantity do not generally occur at the same plume time as each other, or as the counterparts for another physical quantity.

proportional to the effective radius, and this underprediction in r_{eff} would thus lead to an increase in optical depths by 10%. The cloud albedo α is given to a good approximation by *Meador and Weaver* [1980] as

$$\alpha = \frac{(1-g)\tau}{1+(1-g)\tau}, \tag{18}$$

where g is the asymmetry parameter. For the scattering of solar radiation by clouds $g \approx 0.85$. If the original optical depth is 15, a relative error of 10% in r_{eff} translates to an increase in the cloud albedo by 2%. For an optical depth of 10, the corresponding increase in cloud albedo would be 2.3%.

[69] Compared to r_{eff}, the errors in ϵ are comparatively large. Considering that ϵ is the ratio of standard deviation to mean diameter, we found that the large error is introduced by errors in the standard deviation (not the mean diameter).

[70] In summary, the scenario "both" showed the largest deviations from the reference case for all four quantities, f_N, f_{BC}, r_{eff} and ϵ. This is not surprising, since this averaging scenario corresponds to the largest manipulation of the reference aerosol population. Interestingly, even for large plume times t_p, which are usually identified with a high degree of "aging", the error in scenario "both" did not necessarily vanish, as Figure 15a shows. Also, while size-bin averaging consistently resulted in small errors, the magnitude of the error due to composition averaging was larger for f_{BC} than for f_N.

[71] To elucidate the latter we analyzed the cloud droplet population as shown in Figure 16. The solid line in Figure 16a shows f_N for the reference case. The other lines show f_N segregated according to the dry BC mass fraction $w_{BC,dry}$ of the CCN that formed the cloud droplets. The largest contribution (thin solid line) came from aerosol particles with $w_{BC,dry}$ between 0% and 20%. These particles contributed on average 88% of the CDNC during the two days. Aerosol particles with $w_{BC,dry}$ between 20% and 40% (thin dashed line) contributed on average about 10% of the CDNC, and only about 2% of the CDNC were attributed to particles with $w_{BC,dry}$ larger than 40% (thick dashed line). Figures 16b–16d show that while f_N was replicated well for each averaging scenario, only the size-bin-averaging scenario also replicated the information on mixing state well (Figure 16c). Due to the composition averaging in scenarios "comp" and "both", the mixing state information was distorted. In particular, these cases had very few particles with higher w_{BC} compared to the reference case, as evident in Figure 11, leading to the observed differences in f_{BC}.

6.2. Impact of Cooling Rate on the Averaged Simulation Results

[72] We repeated the sets of averaged simulations for the two different cooling rates (0.25 K/min and 1 K/min). The finding shown in Figure 14 for the cooling rate of 0.5 K/min holds for the other cooling rates as well, namely that s_{max} is not impacted by the different averaging scenarios. Table 2 gives a summary of the range of errors for the four different physical quantities. Several studies found a larger sensitivity of CCN properties to the underlying aerosol for small cooling rates (low updraft velocities) [e.g., *Ervens et al.*, 2010]. For our results this applies for some quantities and averaging scenarios, but not for all. A clear dependence on cooling rate for all averaging scenarios was seen for f_{BC} with the largest errors occurring at the lowest cooling rate (−7.2% to 840% for scenario "both" and the cooling rate of 0.25 K/min). For f_N, ϵ and r_{eff} there is not such a clear trend evident.

6.3. Connections to Other Studies

[73] Several prior studies on CCN activation have explored certain aspects of the importance of mixing state. For example, *Kuwata and Kondo* [2008] reported evidence for the occurrence of a particle population with non-uniform mixing states in the urban atmosphere of Tokyo. They pointed out the importance of BC-containing particles in

controlling CCN concentrations in an urban environment with fresh emissions and concluded that particles with large non-volatile cores (presumably consisting of BC) were largely CCN-inactive. This is in agreement with our findings showing that particles with large BC content ($w_{BC,dry} > 40\%$) contribute very little to the CCN concentration, which leads to low values of f_N during early plume hours.

[74] *Medina et al.* [2007] investigated CCN closure for aerosols representing polluted continental conditions from the Great Lakes area during ICARTT 2004. They found that assuming size-dependent composition lead to improved closure but that overprediction still occurred in some instances. Size-dependent composition corresponds to our scenario "both", and we also see an overprediction for f_N for most plume hours since the detailed composition information is lost.

[75] *Wang et al.* [2010] investigated CCN properties for Mexico City. They concluded that the CCN concentration can be derived within 20% assuming internal mixture if a great majority of particles have overall $\kappa > 0.1$ and that the increase of κ to such a value occurs within a few hours during daytime. Our results are broadly consistent with their findings, however we would like to point out that in a polluted environment where emissions age quickly, fresh emissions are likely to be replenished continuously, which can lead to an overestimation of CCN and CDNC concentrations when an internal mixture is assumed.

[76] *Anttila* [2010] performed cloud parcel modeling studies using a sectional model approach with input particle populations based on observational data, including both size and hygroscopicity information. The author showed that assuming an internal mixture for externally mixed urban and rural particle populations lead to errors in CDNC up to 35%, compared to 12% for marine and continental background. While this work is similar in spirit to our study, we have used a reference particle population that fully resolves the complex mixing state of the aerosol, without a priori assumptions. The errors we observed due to averaging are of a similar magnitude to those found by *Anttila* [2010].

[77] An important distinction between studies on CCN closure and our study is that we do not use predefined supersaturation thresholds but rather we include the competition for water vapor. The buffering impact of this is most evident for the early plume hours, when fresh emissions coexist with hygroscopic background particles in separate subpopulations. The averaged simulations lead to some overestimation of f_N, however the error is not as large as one might expect, since the resulting supersaturation is also impacted and in this case it is somewhat lower than in the reference case. These findings are consistent with the results reported in *Cubison et al.* [2008] and *Ervens et al.* [2010], who pointed out that differences in model results and observations were reduced when allowing for feedback of the particles on supersaturation. Further, *Ervens et al.* [2010] concluded that initially hydrophobic particles are sufficiently processed within a few kilometers downwind and that an internal-mixture assumption may be appropriate to obtain closure. However, they added the caveat that this simplified composition may not necessarily represent actual properties. This is confirmed by our findings on the predictions of f_N versus f_{BC}. While the error in f_N was relatively small (within 35% for the base-case cooling rate) for all averaging scenarios, this agreement was obtained for the wrong reasons. This became evident when we predicted another quantity (f_{BC}), for which the error then was much larger.

7. Conclusion

[78] In this study we described the use of the particle-resolved aerosol model PartMC-MOSAIC in conjunction with a cloud parcel model to quantify the importance of mixing state information for cloud droplet activation. We simulated an idealized urban plume scenario tracking the composition of about 10 000 computational particles over the course of 48 hours. We then used the simulated particle populations at each of the 49 hours as input for a 10-minute cloud parcel simulation. These simulated activation and condensational growth of the particle population as the parcel underwent cooling at a prescribed rate and the individual particles competed for water vapor. We used the SUNDIALS implicit BDF solver for the integration of the ODE system describing the cloud parcel.

[79] The maximum supersaturation reached in the individual cloud parcel simulations for the base case of 0.5 K/min ranged between 0.20% and 0.35%. This difference was exclusively caused by differences in the initial aerosol population. The fraction of particles that became cloud droplets generally increased when we initialized the cloud parcel model with particles from the later part of the 48-hour urban plume simulation. While during the morning of the first day the cloud droplet fraction amounted to 20%, this increased to about 70% by the end of the second day. This is consistent with the notion that the aerosol population during the early plume hours contained a large proportion of "fresh" soot particles, which were not easily activated. As a response higher maximum saturation ratios were reached. Over the course of the simulation these particles "aged", hence the cloud droplet fraction increased. The same applied to the BC mass fraction that is nucleation-scavenged.

[80] We then investigated the importance of size information versus composition information for the prediction of cloud droplet number concentration and nucleation-scavenged black carbon mass. From this the following picture emerged for the base-case cooling rate of 0.5 K/min: for the cloud droplet number fraction f_N, both composition averaging and size-bin averaging led to relatively small errors (less than 25% for all 48 cloud parcel simulations). Larger errors (up to 34%) arose for the scenario where we averaged both size and composition. In contrast, for the nucleation-scavenged black-carbon mass f_{BC} the results for size-bin averaging tracked the reference case well, while composition averaging with or without size-bin averaging led to errors of up to 600%. Larger cooling rates lead to smaller errors for all averaging scenarios in f_{BC}, however for f_N, ϵ and r_{eff} no such clear dependence emerged.

[81] These results show that for the conditions simulated here, to accurately simulate black-carbon mass scavenging it is important to resolve the composition distribution within each size bin if fresh emissions coexist with hygroscopic aged emissions or other hygroscopic types of particles,

although we have not quantified how much composition resolution is required. It is less important to resolve the particle composition for determining cloud droplet number fractions. We caution that our study does not take into account the effects of composition and size-bin averaging on the evolution of the urban plume simulation itself, as we used the fully resolved particle population in that case. It is likely that all types of averaging would introduce error in the urban plume evolution, which would then contribute to additional error in the predicted cloud droplet number fraction and nucleation-scavenged black-carbon mass. We note that our results are consistent with those of *Dusek et al.* [2006], which are often stated as "size matters more than composition", as we have considered altering the resolution of size information but we always modeled the size dependence of the aerosol distribution.

[82] There have been a number of modeling and observational studies on the importance of mixing state for CCN activation, including *Cubison et al.* [2008], *Medina et al.* [2007], *Wang et al.* [2010], *Ervens et al.* [2010], *Kuwata and Kondo* [2008], *Dusek et al.* [2006], and *Anttila* [2010]. Common conclusions from these studies are that aerosol populations dominated by fresh emissions need size-resolved composition representation, whereas size-resolved composition is less important for "aged" particles, and that differences in CCN decrease if CDNC are considered. All of these findings are consistent with our study as detailed in Section 6.3. However, we go beyond this as we consider the fact that true aerosol populations have not merely size-dependent composition, but a significant range of compositions at each size. Our results show that adequately predicting CCN number does not generally result in accurate prediction of other quantities, such as scavenged BC fraction. This is reasonable as fitting the CCN spectrum is merely a one-dimensional constraint on a complex multidimensional aerosol population.

Appendix A: Cloud Parcel Model Details

A1. Additional Model Equations

[83] For the saturation vapor pressure P^0 we use the expression according to [*Pruppacher and Klett*, 1997, Appendix to Chapter 4]:

$$P^0(T) = 611\exp\left(17.15\frac{T-273.15}{T-38}\right), \tag{A1}$$

The corrected diffusivity coefficient for particle i, $D'_{v,i}$, is expressed as

$$D'_{v,i} = \frac{D_v}{1+\frac{2D_v}{\alpha}\sqrt{\frac{2\pi M_w}{RT}}/D_i}, \tag{A2}$$

where the diffusivity of water vapor in air is

$$D_v = \frac{0.211\times10^{-4}}{p/p_0}\left(\frac{T}{273}\right)^{1.94}, \tag{A3}$$

and α is the thermal accommodation coefficient, which we take to be $\alpha = 1$. The variables p and p_0 are environmental air pressure and standard surface pressure, respectively. The corrected thermal conductivity for air, $k'_{a,i}$, is given by

$$k'_{a,i} = \frac{k_a}{1+\frac{2k_a}{\alpha\rho_{air}c_p}\sqrt{\frac{2\pi M_{air}}{RT}}/D_i}, \tag{A4}$$

where c_p is specific heat capacity of air at constant pressure, M_{air} is the molecular weight of air, ρ_{air} is the density of air, and k_a is the thermal conductivity of air given by

$$k_a = 10^{-3}(4.39 + 0.071T). \tag{A5}$$

A2. Implications of Assuming Constant Values for κ

[84] Assuming constant κ values throughout the cloud parcel run is a simplification since κ actually depends on the ambient relative humidity (RH). We evaluated the impact of this simplification on our results by conducting additional cloud parcel simulations where we started from different initial RH values as suggested by M. D. Petters (private communication, 2012). If the results of CDNC and nucleation-scavenged BC mass concentration were sensitive to the κ-RH dependence, we would obtain different results of these quantities for simulations with different initial RH conditions. We performed test runs with initial RH of 95%, 97% and 99% using four different initial aerosol populations (t_p = 1, 7, 15, 36). As seen in Figure A1, for each initial aerosol population the resultant CDNC fractions and scavenged BC mass fractions for the three initial RH conditions are within 0.3% of each other. We conclude that the sensitivity of our results to the κ-RH dependence are very small and this effect can be neglected.

A3. Numerical Solution of Cloud Parcel Equations

[85] The system of equations (3), (4), and (7) constitute a Differential-Algebraic Equation (DAE) system. We solved this system in two layers, with a per-particle Newton loop to solve (3) and (4) for $\dot{D}_i$ as a function of D_i and S_v, and then an Ordinary Differential Equation (ODE) solver to solve the system with the state vector $x = \left(S_v, D_1, \ldots, D_{N_p}\right)$.

[86] Rather than solving the implicit equations (3) and (4) for $\dot{D}_i$, it is also possible to use the assumption that $\delta_i \ll 1$ and use a first-order Taylor expansion of the exponential in (3) to obtain an explicit equation for $\dot{D}_i$ [see *Seinfeld and Pandis*, 1997, Equation 17.70]. In a representative test-case we found that this approximate explicit approach reduced the computational cost by about 25%, at the expense of errors of 1.9% in S_{max} and 1.0% in the predicted CCN concentration. We do not expect that the use of the explicit formulation would significantly alter our numerical results.

[87] We used the CVODE solver [*Cohen and Hindmarsh*, 1996] method from SUNDIALS (SUite of Nonlinear and DIfferential/ALgebraic equation Solvers) version 2.4.0 [*Hindmarsh et al.*, 2005], with the backward-differentiation formula (BDF) method and Newton iterations due to the stiffness of the ODE system. For efficient computation we explicitly evaluated the solution of the linear system given by the Newton matrix $M = I - \gamma J$, where I is the identity, γ

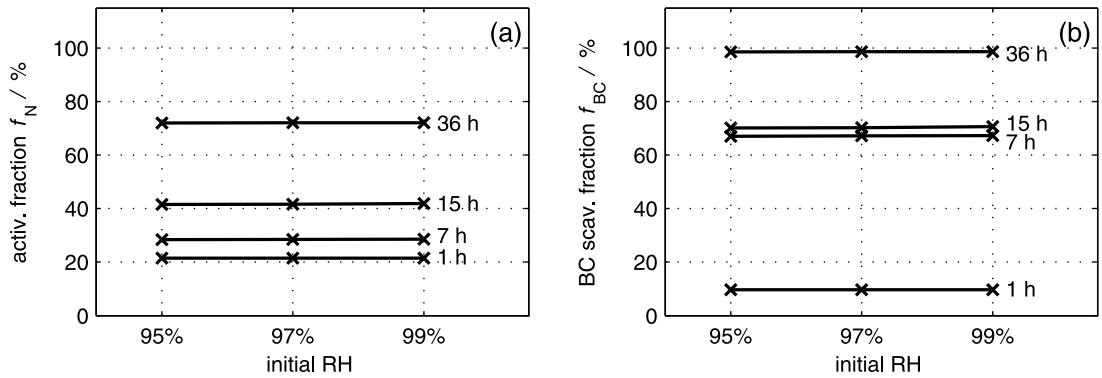

Figure A1. (a) Activation fraction f_N for plume hours t_p = 1, 7, 15, 36 h using three different initial conditions for RH. The base-case cooling rate of 0.5 K/min was used. (b) The same as in Figure A1a, but for nucleation-scavenged BC fraction f_{BC}.

is a scalar parameter, and J is the Jacobian matrix for the ODE system. The Jacobian matrix is very sparse, as $\dot{D}_i$ does not directly depend on D_j for $j \neq i$. We can exploit this fact to explicitly solve the linear system for M, as follows. In block form we have

$$M = \begin{bmatrix} A & B \\ C & D \end{bmatrix} \tag{A6}$$

$$A = 1 - \gamma \frac{\partial \dot{S}_v}{\partial S_v} \qquad B_i = -\gamma \frac{\partial \dot{S}_v}{\partial D_i} \tag{A7}$$

$$C_i = -\gamma \frac{\partial \dot{D}_i}{\partial S_v} \qquad D_{ii} = 1 - \gamma \frac{\partial \dot{D}_i}{\partial D_i} \tag{A8}$$

for $i = 1, \ldots, N_p$ and where we observe that D is diagonal. The solution of the block system

$$\begin{bmatrix} A & B \\ C & D \end{bmatrix} \begin{bmatrix} u \\ v \end{bmatrix} = \begin{bmatrix} p \\ q \end{bmatrix} \tag{A9}$$

can be written using the Schur complement as

$$u = \left(A - BD^{-1}C\right)^{-1}\left(p - BD^{-1}q\right) \tag{A10}$$

$$v = D^{-1}(q - Cu). \tag{A11}$$

As A is 1×1 and D is diagonal, (A10) and (A11) can be evaluated with cost $O(N_p)$. The number of Newton iterations required is independent of N_p, so the total simulation cost of the cloud parcel model is $O(N_p)$ (linear in the number of particles, N_p).

Appendix B: Aerosol Population Averaging

[88] In the following subsections we consider a single size bin containing N_p particles, with particle i, for $i = 1, \ldots, N_p$, containing volume v_i^a of species a, for $a = 1, \ldots, A$. We write v^a for the total volume of species a in all particles within the size bin, v_i for the total volume of particle i, and v for the total volume of all particles in the size bin. These quantities are given by

$$v^a = \sum_{i=1}^{N_p} v_i^a \tag{B1}$$

$$v_i = \sum_{a=1}^{A} v_i^a \tag{B2}$$

$$v = \sum_{a=1}^{A} v^a = \sum_{i=1}^{N_p} v_i = \sum_{i=1}^{N_p} \sum_{a=1}^{A} v_i^a. \tag{B3}$$

B1. Composition Averaging

[89] For scenario "comp" we averaged the composition of the particles within each size bin, which retains the sizes of the individual particles but alters their compositions. The composition-averaged particles have volume $\bar{v}_i^a$ of species a in particle i, defined by

$$\bar{v}_i^a = \frac{v^a v_i}{v}, \tag{B4}$$

for $a = 1, \ldots, A$ and $i = 1, \ldots, N_p$.

[90] This results in per-particle species ratios that are all equal and the same as the total species ratios:

$$\frac{\bar{v}_i^a}{\bar{v}_i} = \frac{v^a v_i}{v} \frac{1}{v_i} = \frac{v^a}{v}, \tag{B5}$$

while the individual particle volumes are preserved:

$$\bar{v}_i = \sum_{a=1}^{A} \bar{v}_i^a = \sum_{a=1}^{A} \frac{v^a v_i}{v} = v_i. \tag{B6}$$

Additionally, the total species volumes are preserved:

$$\bar{v}^a = \sum_{i=1}^{N_p} \bar{v}_i^a = \sum_{i=1}^{N_p} \frac{v^a v_i}{v} = v^a, \tag{B7}$$

the total particle volume are preserved:

$$\bar{v} = \sum_{i=1}^{N_p} \sum_{a=1}^{A} \bar{v}_i^a = \sum_{i=1}^{N_p} v_i = v, \tag{B8}$$

and the particle volume ratios of total volume are preserved:

$$\frac{\bar{v}_i}{\bar{v}} = \frac{v_i}{v}. \tag{B9}$$

B2. Size-Bin Averaging

[91] For scenario "size" we assigned the average particle volume to all particles within each size bin. The size-bin-averaged particles have volume $\hat{v}_i^a$ of species a in particle i, defined by

$$\hat{v}_i^a = \frac{v_i^a}{v_i} \frac{v}{N_p}, \tag{B10}$$

for $a = 1, \ldots, A$ and $i = 1, \ldots, N_p$.

[92] The size-bin-averaging rule gives particle volumes that are the average volume:

$$\hat{v}_i = \sum_{a=1}^{A} \hat{v}_i^a = \sum_{a=1}^{A} \frac{v_i^a}{v_i} \frac{v}{N_p} = \frac{v}{N_p}. \tag{B11}$$

while preserving the per-particle species ratios:

$$\frac{\hat{v}_i^a}{\hat{v}_i} = \frac{\frac{v_i^a}{v_i} \frac{v}{N_p}}{\frac{v}{N_p}} = \frac{v_i^a}{v_i}. \tag{B12}$$

A consequence of size-bin averaging is that the total species volumes are not preserved:

$$\hat{v}^a = \sum_{i=1}^{N_p} \hat{v}_i^a = \sum_{i=1}^{N_p} \frac{v_i^a}{v_i} \frac{v}{N_p} \neq v^a. \tag{B13}$$

However, the total volume is preserved:

$$\hat{v} = \sum_{i=1}^{N_p} \sum_{a=1}^{A} \hat{v}_i^a = \sum_{i=1}^{N_p} \sum_{a=1}^{A} \frac{v_i^a}{v_i} \frac{v}{N_p} = \sum_{i=1}^{N_p} \frac{v}{N_p} = v \tag{B14}$$

and the particle volume ratios of total volume are all equal:

$$\frac{\hat{v}_i}{\hat{v}} = \frac{v/N_p}{v} = \frac{1}{N_p}. \tag{B15}$$

Note that when size-bin averaging a collection of particles within a particular size bin, the average volume assigned to each averaged particle will in general not be the center of the size bin. This is reflected in the fact that the vertical lines in Figure 11 are not evenly spaced.

B3. Both Composition and Size-Bin Averaging

[93] For scenario "both" we averaged first composition and then size within one size bin. This gives the volume of species a in particle i, $\hat{\bar{v}}_i^a$, as

$$\hat{\bar{v}}_i^a = \frac{\bar{v}_i^a}{\bar{v}_i} \frac{\bar{v}}{N_p} = \frac{v^a}{N_p}. \tag{B16}$$

[94] This results in particle volumes that are equal to the average volume:

$$\hat{\bar{v}}_i = \sum_{a=1}^{A} \hat{\bar{v}}_i^a = \sum_{a=1}^{A} \frac{v^a}{N_p} = \frac{v}{N_p} \tag{B17}$$

and per-particle species ratios that are all equal and the same as the total species ratios:

$$\frac{\hat{\bar{v}}_i^a}{\hat{\bar{v}}_i} = \frac{\frac{v^a}{N_p}}{\frac{v}{N_p}} = \frac{v^a}{v}. \tag{B18}$$

In addition, the total species volumes are preserved:

$$\hat{\bar{v}}^a = \sum_{i=1}^{N_p} \hat{\bar{v}}_i^a = \sum_{i=1}^{N_p} \frac{v^a}{N_p} = v^a \tag{B19}$$

and the total volume is preserved:

$$\hat{\bar{v}} = \sum_{i=1}^{N_p} \sum_{a=1}^{A} \hat{\bar{v}}_i^a = \sum_{i=1}^{N_p} \sum_{a=1}^{A} \frac{v^a}{N_p} = \sum_{i=1}^{N_p} \frac{v}{N_p} = v, \tag{B20}$$

which results in the particle volume ratios of total volume being all equal:

$$\frac{\hat{\bar{v}}_i}{\hat{\bar{v}}} = \frac{\frac{v}{N_p}}{v} = \frac{1}{N_p}. \tag{B21}$$

[95] Note that if both averaging techniques are performed, the order of application is significant. In general, if we compute $\hat{\bar{v}}_i^a$ (first composition then size-bin averaging) and $\bar{\hat{v}}_i^a$ (first size-bin then composition averaging), the results will differ, so that $\hat{\bar{v}}_i^a \neq \bar{\hat{v}}_i^a$. We choose to use composition-then-size because size-then-composition results in

$$\bar{\hat{v}}_i^a = \frac{\hat{v}^a \hat{v}_i}{\hat{v}} = \frac{\hat{v}^a}{N_p} \tag{B22}$$

and so total species volumes are not preserved:

$$\bar{\hat{v}}^a = \sum_{i=1}^{N_p} \bar{\hat{v}}_i^a = \sum_{i=1}^{N_p} \frac{\hat{v}^a}{N_p} = \hat{v}^a \neq v^a. \tag{B23}$$

[96] **Acknowledgments.** The authors acknowledge funding from the National Science Foundation under grants NSF ATM 07-39404 and NSF ATM 09-34491. We are grateful to Markus Petters for a suggested method of evaluating the sensitivity to variable κ values, as described in section A2.

References

Abdul-Razzak, H., and S. J. Ghan (2000), A parameterization of aerosol activation: 2. Multiple aerosol types, *J. Geophys. Res.*, *105*, 6837–6844.

Abdul-Razzak, H., S. J. Ghan, and C. Rivera-Carpio (1998), A parameterization of aerosol activation: 1. Single aerosol types, *J. Geophys. Res.*, *103*, 6123–6131.

Adachi, K., S. H. Chung, and P. R. Buseck (2010), Shapes of soot aerosol particles and implications for their effects on climate, *J. Geophys. Res.*, *115*, D15206, doi:10.1029/2009JD012868.

Anttila, T. (2010), Sensitivity of cloud droplet formation to the numerical treatment of the particle mixing state, *J. Geophys. Res.*, *115*, D21205, doi:10.1029/2010JD013995.

Bahadur, R., L. M. Russell, M. Z. Jacobson, K. Prather, A. Nenes, P. Adams, and J. H. Seinfeld (2012), Importance of composition and hygroscopicity

of BC particles to the effects of bc mitigation on cloud properties: Application to california conditions, *J. Geophys. Res.*, *117*, D09204, doi:10.1029/2011JD017265.

Bauer, S., D. Wright, D. Koch, E. Lewis, R. McGraw, L. Chang, S. Schwartz, and R. Ruedy (2008), MATRIX (Multiconfiguration Aerosol TRacker of mIXing state): An aerosol microphysical module for global atmospheric models, *Atmos. Chem. Phys.*, *8*, 6003–6035.

Brenguier, J. L., H. Pawlowska, L. Schüller, R. Preusker, and J. Fisher (2000), Radiative properties of boundary layer clouds: Droplet effective radius versus number concentration, *J. Atmos. Sci.*, *57*, 803–821.

Chen, W., Y. H. Lee, P. J. Adams, A. Nenes, and J. H. Seinfeld (2010), Will black carbon mitigation dampen aerosol indirect forcing?, *Geophys. Res. Lett.*, *37*, L09801, doi:10.1029/2010GL042886.

Chuang, P. Y., R. J. Charlson, and J. H. Seinfeld (1997), Kinetic limitations on droplet formation in clouds, *Nature*, *390*, 594–596.

Cohen, S. D., and A. C. Hindmarsh (1996), CVODE, a stiff/nonstiff ODE solver in C, *Comput. Phys.*, *10*(2), 138–143.

Conant, W., A. Nenes, and J. Seinfeld (2002), Black carbon radiative heating effects on cloud microphysics and implications for aerosol indirect forcing: 1. Extended Köhler theory, *J. Geophys. Res.*, *107*(D21), 4604, doi:10.1029/2002JD002094.

Conant, W., et al. (2004), Aerosol-cloud drop concentration closure in warm cumulus, *J. Geophys. Res.*, *109*, D13204, doi:10.1029/2003JD004324.

Croft, B., U. Lohmann, and K. von Salzen (2005), Black carbon aging in the Canadian Centre for Climate modelling and analysis atmospheric general circulation model, *Atmos. Chem. Phys.*, *5*, 1931–1949, sRef-ID:1680-7324/acp/2005-5-1931.

Cubison, M. J., B. Ervens, G. Feingold, K. S. Docherty, I. M. Ulbrich, L. Shields, K. Prather, S. Hering, and J. L. Jimenez (2008), The influence of chemical composition and mixing state on Los Angeles urban aerosol on CCN number and cloud properties, *Atmos. Chem. Phys.*, *8*, 5649–5667.

DeMott, P., Y. Chen, S. M. Kreidenweis, D. C. Rogers, and D. E. Sherman (1999), Ice formation by black carbon particles, *Geophys. Res. Lett.*, *26*, 2429–2432.

DeVille, R. E. L., N. Riemer, and M. West (2011), Weighted Flow Algorithms (WFA) for stochastic particle coagulation, *J. Comput. Phys.*, *230*(23), 8427–8451, doi:10.1016/j.jcp.2011.07.027.

Dusek, U., et al. (2006), Size matters more than chemistry for cloud-nucleating ability of aerosol particles, *Science*, *312*(5778), 1375–1378.

Ervens, B., G. Feingold, and S. Kreidenweis (2005), Influence of water-soluble organic carbon on cloud drop number concentration, *J. Geophys. Res.*, *110*, D18211, doi:10.1029/2004JD005634.

Ervens, B., et al. (2010), CCN predictions using simplified assumptions of organic aerosol composition and mixing state: a synthesis from six different locations, *Atmos. Chem. Phys.*, *10*, 4795–4807.

Feingold, G. (2003), Modeling of the first indirect effect: Analysis of measurement requirements, *Geophys. Res. Lett.*, *30*(19), 1997, doi:10.1029/2003GL017967.

Feingold, G., W. L. Eberhard, D. E. Veron, and M. Previdi (2003), First measurements of the Twomey indirect effect using ground-based remote sensors, *Geophys. Res. Lett.*, *30*(6), 1287, doi:10.1029/2002GL016633.

Forster, P., et al. (2007), Changes in atmospheric constituents and in radiative forcing, in *Climate Change 2007: The Physical Science Basis. Contribution of Working Group I to the Fourth Assessment Report of the Intergovernmental Panel on Climate Change*, pp. 129–234, Cambridge Univ. Press, Cambridge, U. K.

Fountoukis, C., and A. Nenes (2005), Continued development of a cloud droplet formation parameterization for global climate models, *J. Geophys. Res.*, *110*, D11212, doi:10.1029/2004JD005591.

Ghan, S., N. Laulainen, R. Easter, R. Wagener, S. Nemesure, E. Chapman, Y. Zhang, and R. Leung (2001), Evaluation of aerosol direct radiative forcing in MIRAGE, *J. Geophys. Res.*, *106*(D6), 5317–5334.

Ghan, S. J., C. C. Chuang, and J. E. Penner (1993), A parameterization of cloud droplet nucleation part I: Single aerosol type, *Atmos. Res.*, *30*, 198–221.

Ghan, S. J., C. C. Chuang, R. C. Easter, and J. E. Penner (1995), A parameterization of cloud droplet nucleation part II: Multiple aerosol type, *Atmos. Res.*, *36*, 39–54.

Hansen, J., M. Sato, and R. Ruedy (1997), Radiative forcing and climate response, *J. Geophys. Res.*, *102*, 6831–6864.

Hindmarsh, A. C., P. N. Brown, K. E. Grant, S. L. Lee, R. Serban, D. E. Shumaker, and C. S. Woodward (2005), SUNDIALS: Suite of nonlinear and differential/algebraic equation solvers, *Trans. Math. Softw.*, *31*(3), 363–396, doi:10.1145/1089014.1089020.

Hitzenberger, R., et al. (1999), Contribution of carbonaceous material to cloud condensation nuclei concentrations in European background (Mt. Sonnblick) and urban (Vienna) aerosols, *Atmos. Environ.*, *33*, 2647–2659.

Howell, W. E. (1949), The growth of cloud drops in uniformly cooled air, *J. Meteorol.*, *6*, 134–149.

Jacobson, M. Z. (1997), Development and application of a new air pollution modeling system — II. Aerosol module structure and design, *Atmos. Environ.*, *31*, 131–144.

Jacobson, M. Z. (2001), Strong radiative heating due to the mixing state of black carbon in atmospheric aerosols, *Nature*, *409*, 695–697.

Kleeman, M., J. Schauer, and G. Cass (2000), Size and composition distribution of fine particulate matter emitted from motor vehicles, *Environ. Sci. Technol.*, *34*, 1132–1142, doi:10.1021/es981276y.

Koch, D., and A. D. D. Genio (2010), Black carbon semi-direct effects on cloud cover: Review and synthesis, *Atmos. Chem. Phys.*, *10*, 7685–7696.

Köhler, H. (1936), The nucleus in and the growth of hygroscopic droplets, *Trans. Faraday Soc.*, *32*, 1152–1161.

Kreidenweis, S., et al. (2003), Modification of aerosol mass and size distribution due to aqueous-phase SO_2 oxidation in clouds: Comparisons of several models, *J. Geophys. Res.*, *108*(D7), 4213, doi:10.1029/2002JD002697.

Kristjansson, J. E. (2002), Studies of the aerosol indirect effect from sulfate and black carbon aerosols, *J. Geophys. Res.*, *107*(D15), 4246, doi:10.1029/2001JD000887.

Kuwata, M., and Y. Kondo (2008), Dependence of size-resolved CCN spectra on the mixing state of nonvolatile cores observed in Tokyo, *J. Geophys. Res.*, *113*, D19202, doi:10.1029/2007JD009761.

Lee, I. Y., G. Hanel, and H. R. Pruppacher (1980), A numerical determination of the evolution of cloud drop spectra due to condensation on natural aerosol particles, *J. Atmos. Sci.*, *37*, 1839–1853.

Liu, Y., and P. H. Daum (2000), Spectral dispersion of cloud droplet size distributions and the parameterization of cloud droplet effective radius, *Geophys. Res. Lett.*, *27*, 1903–1906.

Liu, Y., and P. H. Daum (2002), Indirect warming effect from dispersion forcing, *Nature*, *419*, 580–581.

Majeed, M. A., and A. S. Wexler (2001), Microphysics of aqueous droplets in clouds and fogs as applied to PM-fine modeling, *Atmos. Environ.*, *35*, 1639–1653.

McComiskey, A., G. Feingold, A. S. Frisch, D. D. Turner, M. A. Miller, J. C. Chiu, Q. Min, and J. A. Ogren (2009), An assessment of aerosol-cloud interactions in marine stratus clouds based on surface remote sensing, *J. Geophys. Res.*, *114*, D09203, doi:10.1029/2008JD011006.

McFarquhar, G. M., and A. J. Heymsfield (2001), Parameterization of INDOEX microphysical measurements and calculations of cloud susceptibility: Applications for climate stuides, *J. Geophys. Res.*, *106*(22), 28,675–28,698.

Meador, W. E., and W. R. Weaver (1980), Two-stream approximations to radiative transfer in planetary atmospheres: A unified description of existing methods and a new improvement, *J. Atmos. Sci.*, *37*, 630–643.

Medalia, A., and D. Rivin (1982), Particulate carbon and other components of soot and carbon black, *Carbon*, *20*, 481–492.

Medina, J., A. Nenes, R.-E. P. Sotiropoulou, L. D. Cottrell, L. D. Ziemba, P. J. Beckman, and R. J. Griffin (2007), Cloud condensation nuclei closure during the International Consortium for Atmospheric Research on Transport and Transformation 2004 campaign: Effects of size-resolved composition, *J. Geophys. Res.*, *112*, D10S31, doi:10.1029/2006JD007588.

Ming, Y., V. Ramaswamy, L. J. Donner, and V. T. J. Phillips (2006), A new parameterization of cloud droplet activation applicable to general circulation models, *J. Atmos. Sci.*, *63*, 1348–1356.

Moffet, R., and K. Prather (2009), In-situ measurements of the mixing state and optical properties of soot with implications for radiative forcing estimates, *Proc. Natl. Acad. Sci. U. S. A.*, *106*(29), 11,872–11,877.

Möhler, O., et al. (2005), Effect of sulfuric acid coating on heterogeneous ice nucleation by soot aerosol particles, *J. Geophys. Res.*, *110*, D11210, doi:10.1029/2004JD005169.

Mordy, W. (1959), Computations of the growth by condensation of a population of cloud droplets, *Tellus*, *11*, 16–44.

Nenes, A., and J. H. Seinfeld (2003), Parameterization of cloud droplet formation in global climate models, *J. Geophys. Res.*, *108*(D14), 4415, doi:10.1029/2002JD002911.

Nenes, A., S. Ghan, H. Abdul-Razzak, P. Chuang, and J. H. Seinfeld (2001), Kinetic limitations on cloud droplet formation and impact on cloud albedo, *Tellus, Ser. B*, *53*, 133–149.

Nenes, A., W. C. Conant, and J. H. Seinfeld (2002), Black carbon radiative heating effects on cloud microphysics and implications for the aerosol indirect effect: 2. Cloud microphysics, *J. Geophys. Res.*, *107*(D21), 4605, doi:10.1029/2002JD002101.

Peng, Y., U. Lohmann, R. Leaitch, C. Banic, and M. Couture (2002), The cloud albedo-cloud droplet effective radius relationship for clean and polluted clouds from RACE and FIRE.ACE, *J. Geophys. Res.*, *107*(D11), 4106, doi:10.1029/2000JD000281.

Petters, M., A. Prenni, S. Kreidenweis, P. DeMott, A. Matsunaga, Y. Lim, and P. Ziemann (2006), Chemical aging and the hydrophobic-to-hydrophilic conversion of carbonaceous aerosol, *Geophys. Res. Lett.*, *33*, L24806, doi:10.1029/2006GL027249.

Petters, M. D., and S. M. Kreidenweis (2007), A single parameter representation of hygroscopic growth and cloud condensation nucleus activity, *Atmos. Chem. Phys.*, *7*, 1961–1971.

Petters, M. D., and S. M. Kreidenweis (2008), A single parameter representation of hygroscopic growth and cloud condensation nucleus activity — Part 2: Including solubility, *Atmos. Chem. Phys.*, *8*, 6273–6279.

Prenni, A., M. Petters, S. Kreidenweis, P. DeMott, and P. Ziemann (2007), Cloud droplet activation of secondary organic aerosol, *J. Geophys. Res.*, *112*, D10223, doi:10.1029/2006JD007963.

Pruppacher, H. R., and J. D. Klett (1997), *Microphysics of Clouds and Precipitation*, Kluwer Acad., Dordrecht, Netherlands.

Riemer, N., H. Vogel, B. Vogel, and F. Fiedler (2003), Modeling aerosols on the mesoscale-γ: Treatment of soot aerosol and its radiative effects, *J. Geophys. Res.*, *108*(D19), 4601, doi:10.1029/2003JD003448.

Riemer, N., H. Vogel, and B. Vogel (2004), Soot aging time scales in polluted regions during day and night, *Atmos. Chem. Phys.*, *4*, 1885–1893.

Riemer, N., M. West, R. Zaveri, and R. Easter (2009), Simulating the evolution of soot mixing state with a particle-resolved aerosol model, *J. Geophys. Res.*, *114*, D09202, doi:10.1029/2008JD011073.

Riemer, N., M. West, R. Zaveri, and R. Easter (2010), Estimating black carbon aging time-scales with a particle-resolved aerosol model, *J. Aerosol Sci.*, *41*, 143–158.

Rotstayn, L. D., and Y. Liu (2003), Sensitivity of the first indirect aerosol effect to an increase of cloud droplet spectral dispersion with droplet number concentration, *J. Clim.*, *16*, 3476–3481.

Schell, B., I. J. Ackermann, F. S. Binkowski, and A. Ebel (2001), Modeling the formation of secondary organic aerosol within a comprehensive air quality model system, *J. Geophys. Res.*, *106*, 28,275–28,293.

Schwarz, J., et al. (2008), Measurement of the mixing state, mass, and optical size of individual black carbon particles in urban and biomass burning emissions, *Geophys. Res. Lett.*, *35*, L13810, doi:10.1029/2008GL033968.

Segal, Y., and A. Khain (2006), Dependence of droplet concentration on aerosol conditions in different cloud types: Application to droplet concentration parameterization of aerosol conditions, *J. Geophys. Res.*, *111*, D15204, doi:10.1029/2005JD006561.

Seinfeld, J. H., and S. Pandis (1997), *Atmospheric Chemistry and Physics: From Air Pollution to Climate Change*, John Wiley, New York.

Spracklen, D. V., K. S. Carslaw, U. Pöschl, A. Rap, and P. M. Forster (2011), Global cloud condensation nuclei influenced by carbonaceous combustion aerosol, *Atmos. Chem. Phys.*, *11*, 9067–9087.

Stier, P., et al. (2005), The aerosol-climate model ECHAM5-HAM, *Atmos. Chem. Phys.*, *5*, 1125–1156.

Toner, S., S. Sodeman, and K. Prather (2006), Single particle characterization of ultrafine and accumulation mode particles from heavy duty diesel vehicles using aerosol time-of-flight mass spectrometry, *Environ. Sci. Technol.*, *40*, 3912–3921, doi:10.1021/es051455x.

Twohy, C. H., M. D. Petters, J. R. Snider, B. Stevens, W. Tahnk, M. Wetzel, L. Russell, and F. Burnet (2005), Evaluation of the aerosol indirect effect in marine stratocumulus clouds: Droplet number, size, liquid water path, and radiative impact, *J. Geophys. Res.*, *110*, D08203, doi:10.1029/2004JD005116.

Twomey, S. (1974), Pollution and the planetary albedo, *Atmos. Environ.*, *8*, 1251–1256.

Wang, J., M. Cubison, A. Aiken, J. Jimenez, and D. Collins (2010), The importance of aerosol mixing state and size-resolved composition on CCN concentration and the variation of the importance with atmospheric aging of aerosols, *Atmos. Chem. Phys.*, *10*, 7267–7283.

Weingartner, E., H. Burtscher, and H. Baltensperger (1997), Hygroscopic properties of carbon and diesel soot particles, *Atmos. Environ.*, *31*, 2311–2327.

Zaveri, R. A., and L. K. Peters (1999), A new lumped structure photochemical mechanism for large-scale applications, *J. Geophys. Res.*, *104*, 30,387–30,415.

Zaveri, R. A., R. C. Easter, and L. K. Peters (2005a), A computationally efficient multicompoent equilibrium solver for aerosols (MESA), *J. Geophys. Res.*, *110*, D24203, doi:10.1029/2004JD005618.

Zaveri, R. A., R. C. Easter, and A. S. Wexler (2005b), A new method for multicomponent activity coefficients of electrolytes in aqueous atmospheric aerosols, *J. Geophys. Res.*, *110*, D02201, doi:10.1029/2004JD004681.

Zaveri, R. A., R. C. Easter, J. D. Fast, and L. K. Peters (2008), Model for simulating aerosol interactions and chemistry (MOSAIC), *J. Geophys. Res.*, *113*, D13204, doi:10.1029/2007JD008782.

Zaveri, R. A., J. C. Barnard, R. C. Easter, N. Riemer, and M. West (2010), Particle-resolved simulation of aerosol size, composition, mixing state, and the associated optical and cloud condensation nuclei activation properties in an evolving urbanplume, *J. Geophys. Res.*, *115*, D17210, doi:10.1029/2009JD013616.